

Three Dimensional Magneto Hydrodynamical Simulations of Gravitational Collapse of a $15M_{\odot}$ Star

Takami Kuroda and Hideyuki Umeda

Department of Astronomy, School of Science, University of Tokyo, Bunkyo-ku, Tokyo, 113-0033, Japan; kuroda@astron.s.u-tokyo.ac.jp, umeda@astron.s.u-tokyo.ac.jp,

ABSTRACT

We introduce our newly developed two different, three dimensional magneto hydrodynamical codes in detail. One of our codes is written in the Newtonian limit (NMHD) and the other is in the fully general relativistic code (GRMHD). Both codes employ adaptive mesh refinement and, in GRMHD, the metric is evolved with the "Baumgarte-Shapiro-Shibata-Nakamura" formalism known as the most stable method at present. We did several test problems and as for the first practical test, we calculated gravitational collapse of a $15M_{\odot}$ star. Main features found from our calculations are; (1) High velocity bipolar outflow is driven from the proto-neutronstar and moves through along the rotational axis in strongly magnetized models; (2) A one-armed spiral structure appears which is originated from the low- $|T/W|$ instability; (3) By comparing GRMHD and NMHD models, the maximum density increases about $\sim 30\%$ in GRMHD models due to the stronger gravitational effect. These features agree very well with previous studies and our codes are thus reliable to numerical simulation of gravitational collapse of massive stars.

Subject headings: Methods: numerical — MHD — stars: magnetars — supernovae: general

1. Introduction

There are lots of works searching for the explosion mechanisms of core-collapse supernovae (CCSNe), however we have still not obtained any conclusive results in these decades. Recent works, both observational and theoretical ones, show several indications that their explosions are commonly aspherical. For instance, Maeda et al. (2008) obtained late-time spectra for a lot of CCSNe and showed that the explosion morphologies of stars without H envelope are close to bipolar configurations. Furthermore, non-axisymmetric explosion is found from the observation of SN 2005bf by Tanaka et al. (2009b). In their report, they presented an optical spectropolarimetric observation of Type Ib supernova 2005bf and claimed that SN 2005bf can be explained as unipolar

explosion and also the direction of launched unipolar blob is tilted from the symmetric axis. Therefore, the asphericities might be key ingredients to understand the explosion mechanisms, especially for a subset class of CCSNe such as Type Ib SNe. These asphericities found from the observations are thought to be products of hydrodynamical instabilities occurring in the vicinity of the proto neutronstars (PNSs). From the previous theoretical/numerical works, it is widely known that there are many types of hydrodynamical instabilities which would occur during CCSNe, such as: the Ledoux convection (Keil et al. 1996): vortical-acoustic instability (Blondin et al. 2003): magneto hydrodynamical instabilities, e.g., Magneto Rotational Instability (MRI) (Balbus & Hawley 1991; Akiyama et al. 2003; Obergaulinger et al. 2009) or Kelvin Helmholtz instability: rotational instabilities, e.g., dynamical bar-mode instability (Rampp et al. 1998; Shibata et al. 2003), secular instability (Imamura et al. 2003), low- $|T/W|$ instability (Shibata et al. 2003; Watts et al. 2005; Ott et al. 2005). Which of these instabilities would occur depends on progenitor mass, the rotational/magnetic field velocity configuration, the interaction between matters and neutrinos, etc.

Among these mechanisms, rotational instabilities are common byproducts of relatively fast-spinning progenitors and their subsequent collapses. If ratio of rotational to gravitational potential energy $\beta \equiv |T/W|$, at core bounce, exceeds $\beta_{\text{dyn}} \sim 0.27$ then the dynamical bar-mode instability appears (Rampp et al. 1998; Shibata et al. 2003). Simple estimate, in which we assume the angular momentum is almost conserved during core collapse, gives us a rough lower limit of the central angular velocity Ω_c , at pre-collapse stage which exceeds ~ 10 rad/s. Such rotational speed is at least ~ 10 times faster than the results of recent stellar evolutionary calculations (Yoon & Langer 2005). Even if progenitor does not spin so rapidly at the beginning, the secular instability may be appeared if $\beta \gtrsim \beta_{\text{sec}} \sim 0.14$ and also if some dissipative mechanisms exist such as the viscosity, the neutrino radiation or the gravitational radiation reaction (Imamura et al. 2003). Recently, another interesting rotational instability is reported to occur in CCSNe which is the low- $|T/W|$ instability (Shibata et al. 2003; Watts et al. 2005; Ott et al. 2005). This is the resonance instability across the corotation point inside the differentially rotating area and occurs with more reasonable value $\beta \sim 0.01$ or with relatively slow initial spin rate $\Omega_c \sim 1$ rad/s. Such a slow rotation is more realistic compared to aforementioned two mechanisms.

These rotational instabilities are intrinsically three dimensional, non-axisymmetric phenomena. In the ideal MHD limit, which is a reasonable assumption in the CCSNe context, the non axisymmetric motion always convert the toroidal magnetic field into the poloidal component by dragging the toroidal magnetic field. Then, if the differential rotation exists, the converted poloidal magnetic field is again converted back into the toroidal ones. Such a closed cycle never takes place in the axisymmetric motion and may play important roles to amplify magnetic field via, e.g., the dynamo mechanism (Thompson & Duncan 1993) or the MRI. Strongly amplified magnetic field ($\gtrsim 10^{15-16}$ G) launches high velocity outflow along the rotational axis (Mikami et al. 2008) due to the magneto-spring or the magneto-centrifugal effects (Wheeler et al. 2002) and may leave highly magnetized ($\sim 10^{15-16}$ G at surface) neutronstar which is a so-called "magnetar" (Duncan & Thompson 1992). Another feature of the magneto-rotational explosion is, through

these magneto-rotational effects, the explosion morphology becomes highly aspherical. Since the explosion morphology shows stronger asphericity in case of energetic explosion such as Hypernova (HN) or SN associated with gamma-ray burst (GRB) (Maeda et al. 2008), the magneto rotational effects are considered to be more important to such hyper energetic CCSNe than the normal ones.

As just described, the non axisymmetric effects may play important roles and should be examined by three dimensional numerical simulations. However, up to the present date, there are only a few numerical works about CCSNe with three dimensional MHD (see, e.g., Scheidegger et al. (2008, 2009); Mikami et al. (2008)). In Scheidegger et al. (2009), they calculated a number of numerical models aiming for the gravitational wave signature during core collapse, including two types of realistic EOSs, various magnetic-rotational configurations and a neutrino parametrization/leakage scheme. In their work, they showed the low- $|T/W|$ instability appears when the progenitor rotates 2π rad/s or faster and alters the gravitational wave radiation. As for the explosion dynamics, they reported that bipolar outflow is driven by strong magnetic field if the initial central magnetic field strength is the order of $\gtrsim \mathcal{O}(10^{12})\text{G}$ (Mikami et al. 2008; Scheidegger et al. 2009). This is because the magnetic field of the order of $\gtrsim \mathcal{O}(10^{12})\text{G}$ is easily amplified, a factor of $\sim \mathcal{O}(10^{3-4})$ (Burrows et al. 2007), simply by the compression and the rotational winding effects during core collapse. Magnetic pressure with $B \sim 10^{15-16}\text{G}$ is comparable to matter pressure in the vicinity of the surface of PNS and thus drives bipolar outflow. The amplification factor ($\sim \mathcal{O}(10^{3-4})$) hardly depends on the initial strength unless some other nonlinear amplification mechanisms work. In the 3D context however the non axisymmetric motion may trigger the previously mentioned nonlinear amplification mechanisms (e.g., MRI) and may alter the amplification factor or the time scale comparing to axisymmetric motion. Therefore, especially when the initial magnetic field is much weaker than $\sim \mathcal{O}(10^{12})\text{G}$, the axisymmetric assumption may not be suitable for the CCSNe. Additionally, since the strength of the order of $\sim \mathcal{O}(10^{12})\text{G}$ is considered to be unrealistically strong for pre-collapse stage, it should be examined how the initially weak (or more realistic) magnetic field, e.g., $\sim \mathcal{O}(10^9)\text{G}$, is amplified and whether it affects the explosion dynamics or not.

Another challenge for numerical simulations of CCSNe is the treatment of general relativistic effects. Since the gravity plays intrinsic role and also some very massive progenitors ($\gtrsim 25M_{\odot}$, see, Tanaka et al. (2009a)) form black holes (BHs), we cannot say any conclusive results about the explosion mechanisms of CCSNe without taking account of the general relativity (GR). As same as the context of 3D MHD works of CCSNe, there are not so many works done by MHD simulations including GR effects (see, e.g., Shibata et al. (2006); Cerdá-Durán et al. (2007)) and furthermore 3D GRMHD works of CCSNe have not been done yet.

In this paper, we describe our newly developed two 3D-MHD codes for CCSNe simulation. Their features are as follows. Both codes employ adaptive mesh refinement (AMR) technique and can cover wide dynamical ranges from the central compact object ($\sim 10\text{km}$) to beyond the several times of iron core radius ($\sim 10000\text{km}$) or more. Self gravity is included in the Newtonian approximated MHD code and the dynamical metric is included in GRMHD code. High resolution shock capturing scheme is adopted in both codes and can handle the shock discontinuity without

numerical viscosity. We use the staggered mesh algorithm and adopt the Constrained-Transport method to evolve the magnetic field. We have done many test problems and confirmed their abilities.

This paper is organized as follows. From Sec. 2 to 4, we describe our numerical codes, their detailed properties and adopted techniques. In Sec.5 and 6, we report several numerical tests of Newtonian approximated and general relativistic codes, respectively. Section 7 shows our first core-collapse supernovae calculations and their initial setups. We summarize in section 8. We adopt cgs units for NMHD code and geometrical units for GRMHD code in which $G = c = 1$. In our practical calculations of a collapse of $15M_{\odot}$ star, in Sec. 7, physical quantities are notated in cgs units. Greek/Latin indices run through 0-3/1-3.

2. NMHD Code

Our NMHD code solves ideal NMHD equations written in conservative forms together with source terms of self gravity, which are written in the following form:

$$\frac{\partial \mathbf{Q}}{\partial t} + \nabla \cdot \mathbf{F} = \mathbf{S} \quad (1)$$

and Poisson's equation for gravitational potential

$$\nabla^2 \Phi = 4\pi G \rho \quad (2)$$

Where, in Eq. (1)

$$\mathbf{Q} = \begin{bmatrix} \rho \\ \rho \mathbf{u} \\ E \\ \mathbf{B} \end{bmatrix} \quad (3)$$

$$\mathbf{F} = \begin{bmatrix} \rho \mathbf{u} \\ \rho \mathbf{u} \mathbf{u} + \left(P_{\text{tot}} + \frac{\mathbf{B} \cdot \mathbf{B}}{8\pi}\right) \mathbf{I} - \frac{\mathbf{B} \mathbf{B}}{4\pi} \\ \left(E + P_{\text{tot}} + \frac{\mathbf{B} \cdot \mathbf{B}}{8\pi}\right) \mathbf{u} - \frac{(\mathbf{u} \cdot \mathbf{B}) \mathbf{B}}{4\pi} \\ \mathbf{u} \mathbf{B} - \mathbf{B} \mathbf{u} \end{bmatrix} \quad (4)$$

$$\mathbf{S} = \begin{bmatrix} 0 \\ -\rho \nabla \Phi \\ -\rho \mathbf{u} \cdot \nabla \Phi \\ 0 \end{bmatrix} \quad (5)$$

Eq. (1) represents the conservation of mass, momentum, energy and the Faraday's law. ρ , \mathbf{u} , \mathbf{B} , E , P_{tot} , Φ and \mathbf{I} are rest-mass density, fluid velocity, magnetic field, energy density, total pressure, gravitational potential and 3×3 unit matrix, respectively. The energy density and the total pressure are expressed as

$$E = \rho\varepsilon + \frac{\rho\mathbf{u}^2}{2} + \frac{\mathbf{B}^2}{8\pi} \quad (6)$$

$$P_{\text{tot}} = p + \frac{\mathbf{B}^2}{8\pi} \quad (7)$$

Here, p and ε are gas pressure and internal energy density, respectively, and are related via the equation of state, $p = p(\rho, \varepsilon)$. We also define primitive variables $\mathbf{P} \equiv (\rho, \mathbf{u}, \varepsilon, \mathbf{B})$ which is uniquely obtained from conservative variables \mathbf{Q} via EOS. We employ staggered mesh and all variables except magnetic field are defined at cell center while, for instance, $B_x(i, j, k)$ is defined in cell surface $(i+1/2, j, k)$. Hereafter we use $\mathbf{B}' = \mathbf{B}/\sqrt{4\pi}$ and do not express " ' ", unless otherwise stated.

To solve time dependent equation (1), in our cartesian Eulerian grid, we adopt Roe-type upwind solver in which numerical flux $\tilde{\mathbf{F}}$ is defined in cell surface (see Fig.1). Following Powell et al. (1999),

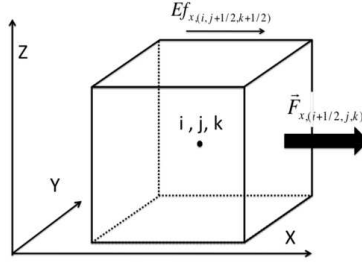


Fig. 1.— Positions where numerical flux and electric field are defined. For instances, x directional numerical flux \mathbf{F}_x is defined at $(i+1/2, j, k)$ and x component of electric field $\mathbf{E}\mathbf{f}_x$ is defined at $(i, j+1/2, k+1/2)$.

$\tilde{\mathbf{F}}$ is constructed from the spectral decomposition of the system and expressed as

$$\tilde{\mathbf{F}} = \left[(\mathbf{F}(\mathbf{P}_L) + \mathbf{F}(\mathbf{P}_R)) - \sum_{m=1}^7 \mathbf{L}_m \cdot (\mathbf{Q}_R - \mathbf{Q}_L) |\lambda_m| \mathbf{R}_m \right] / 2 \quad (8)$$

Here the index L/R represents position immediate left/right of the cell boundary, i.e., when we evaluate the numerical flux at $(i+1/2, j, k)$, the position L and R stand for $(i+1/2-0, j, k)$ and $(i+1/2+0, j, k)$, respectively. $\mathbf{L}_m/\mathbf{R}_m$ and λ_m correspond to left/right eigenvectors and eigenvalues of the system, respectively, and defined in cell surface. Originally, in Powell et al. (1999), they decompose the system into eight spectral modes in which one mode carries the monopole moment of magnetic field. Meanwhile, we adopt the constrained transport method for time evolution of magnetic field and we thus consider only seven modes in our NMHD code (for explicit expressions of seven eigenvectors, see (Ryu et al. 1995)). Eigenvalues λ_m are defined as

$$\lambda_m = (u - c_f, u - c_A, u - c_s, u, u + c_s, u + c_A, u + c_f) \quad (9)$$

Here u is the fluid velocity normal to cell boundary; c_f the fast magnetosonic speed; c_s the slow magnetosonic speed; c_A the *Alfvén* speed. c_A , c_f , c_s are expressed by

$$c_A = B_n / \sqrt{\rho} \quad (10)$$

$$c_{f,s} = \sqrt{\frac{a^2 + \mathbf{B}^2/\rho \pm \sqrt{(a^2 + \mathbf{B}^2/\rho)^2 - 4a^2 c_A^2}}{2}} \quad (11)$$

Where, f/s takes $+/-$ in Eq. (11), B_n represents magnetic field component normal to cell boundary and a is the speed of sound. The speed of sound a in a general form of EOS can be defined by

$$a = \sqrt{\left(p/\rho^2 - \frac{\partial \varepsilon}{\partial \rho}\right) \left(\frac{\partial \varepsilon}{\partial p}\right)^{-1}} \quad (12)$$

Since we define the conservative variables other than magnetic field at cell center, we have to interpolate to obtain those values at immediate left/right of cell boundary. As for the interpolation, we adopt the monotonized central (MC) method (Van Leer 1977) as

$$\begin{aligned} \mathbf{P}_{i\pm 1/2\mp 0} &= \mathbf{P}_i \pm \text{MC}(\mathbf{P}_{i+1} - \mathbf{P}_i, \mathbf{P}_i - \mathbf{P}_{i-1}) \\ \text{MC}(x, y) &= \begin{cases} 2 \text{ sign}(x) \min(|x|, |y|, |x+y|/4) & \text{for } xy > 0 \\ 0 & \text{otherwise} \end{cases} \end{aligned} \quad (13)$$

Additionally, we employ total variational diminishing (TVD) scheme which has second order convergence in space (see Ryu et al. (1995)) and we briefly summarize how we implement it into our NMHD code below. In TVD scheme, summation respect to the spectral modes in Eq. (8) is modified as

$$\sum_{m=1}^7 \mathbf{L}_m \cdot (\mathbf{Q}_R - \mathbf{Q}_L) |\lambda_m| \mathbf{R}_m = \sum_{m=1}^7 \left(Q_l \left(\frac{\Delta t}{\Delta x} \lambda_m + \gamma_m \right) LdQ_{m,i} - (g_l + g_r) \right) \mathbf{R}_m \quad (14)$$

In Eq. (14) we consider x directional numerical flux $\tilde{\mathbf{F}}_{x,i+1/2}$ defined at $(i+1/2, j, k)$ and

$$LdQ_{m,i} = \mathbf{L}_m \cdot (\mathbf{Q}_{i+1/2+0} - \mathbf{Q}_{i+1/2-0}) \quad (15)$$

$$g_i = \frac{LdQ_{m,i}}{2} \left(Q_l \left(\frac{\Delta t}{\Delta x} \lambda_m \right) - \left(\frac{\Delta t}{\Delta x} \lambda_m \right)^2 \right) \quad (16)$$

$$g_r = \text{sign}(g_{i+1}) \max[0, \min(|g_{i+1}|, g_i \text{sign}(g_{i+1}))] \quad (17)$$

$$g_l = \text{sign}(g_i) \max[0, \min(|g_i|, g_{i-1} \text{sign}(g_i))] \quad (18)$$

$$\gamma_m = \begin{cases} (g_r - g_l)/LdQ_{m,i} & \text{for } LdQ_{m,i} \neq 0 \\ 0 & \text{otherwise} \end{cases} \quad (19)$$

$$Q_l(x) = \begin{cases} \frac{x^2}{4\varepsilon} + \varepsilon & \text{for } |x| < 2\varepsilon \\ |x| & \text{for } |x| \geq 2\varepsilon \end{cases} \quad (20)$$

$$\varepsilon = \begin{cases} 0.01 & \text{for } m = 1, 7 \\ 0.1 & \text{for } m = 2, 6 \\ 0.1 & \text{for } m = 3, 5 \\ 0 & \text{for } m = 4 \end{cases} \quad (21)$$

After we obtain the numerical fluxes in all sides of cell, the conservative variables other than magnetic field are updated through predictor and corrector steps (Press et al. 1992). In predictor step, \mathbf{Q}^n is updated from time level n to $n + 1/2$ by $\Delta t/2$, i.e.,

$$\mathbf{Q}^{n+1/2} = \mathbf{Q}^n + 0.5\Delta t \left(-\frac{\tilde{\mathbf{F}}_{x,i+1/2}^n - \tilde{\mathbf{F}}_{x,i-1/2}^n}{\Delta x} - \frac{\tilde{\mathbf{F}}_{y,j+1/2}^n - \tilde{\mathbf{F}}_{y,j-1/2}^n}{\Delta y} - \frac{\tilde{\mathbf{F}}_{z,k+1/2}^n - \tilde{\mathbf{F}}_{z,k-1/2}^n}{\Delta z} + \mathbf{S}_{i,j,k}^n \right) \quad (22)$$

and in corrector step from time level n to $n + 1$ by Δt with using predicted values, i.e.,

$$\mathbf{Q}^{n+1} = \mathbf{Q}^n + \Delta t \left(-\frac{\tilde{\mathbf{F}}_{x,i+1/2}^{n+1/2} - \tilde{\mathbf{F}}_{x,i-1/2}^{n+1/2}}{\Delta x} - \frac{\tilde{\mathbf{F}}_{y,j+1/2}^{n+1/2} - \tilde{\mathbf{F}}_{y,j-1/2}^{n+1/2}}{\Delta y} - \frac{\tilde{\mathbf{F}}_{z,k+1/2}^{n+1/2} - \tilde{\mathbf{F}}_{z,k-1/2}^{n+1/2}}{\Delta z} + \mathbf{S}_{i,j,k}^{n+1/2} \right) \quad (23)$$

This method is second order convergence with respect to time.

On the other hand, as for the time evolution of magnetic field \mathbf{B} , we adopt the constrained transport (CT) scheme (Balsara & Spicer 1999) in which \mathbf{B} is evolved as

$$\frac{\partial \mathbf{B}}{\partial t} = \nabla \times \mathbf{E} \quad (24)$$

Electric field \mathbf{E} for CT scheme is defined at the cell edge (see Fig.1) and is evaluated from Roe-type numerical flux, Eq. (8), with appropriate interpolation. We simply express the electric field as

$$E_{x,i,j+1/2,k+1/2} = \left(\tilde{\mathbf{F}}_{y,i,j+1/2,k}^6 + \tilde{\mathbf{F}}_{y,i,j+1/2,k+1}^6 - \tilde{\mathbf{F}}_{z,i,j,k+1/2}^7 - \tilde{\mathbf{F}}_{z,i,j+1,k+1/2}^7 \right) / 4 \quad (25)$$

Here the upper suffixes in the right hand side denote components of the numerical flux. y and z components of the electric field are obtained straightforwardly by permutation as $x \rightarrow y$, $y \rightarrow z$, $z \rightarrow x$ and $x \rightarrow z$, $y \rightarrow x$, $z \rightarrow y$, respectively.

In self gravitating system, the source term contains gravitational potential which is obtained by solving Poisson equation (our method to solve Poisson equation with AMR framework is described in Sec. 4.2). Since solving Poisson equation is very time consuming task, we solve it only once in one hydrodynamical time step (Truelove et al. 1998) after predictor step is completed. Practically, in predictor step, we extrapolate gravitational potential Φ^n at n th time level via $\Phi^n = (3\Phi^{n-1/2} - \Phi^{n-3/2})/2$ and then predict variables at $(n+1/2)$ th time level through Eq. (22). After the predictor step is completed, we solve Poisson equation by using $\rho^{n+1/2}$. In corrector step, we fully evolve the n th time level to $(n+1)$ th variables by using $\mathbf{Q}^{n+1/2}$ and $\Phi^{n+1/2}$. Even though we extrapolate gravitational potential at n th time level, our numerical results do not show any large error in conservation of energy and numerical convergence is also achieved (described later in Sec. 5.3).

On a final note, we mention about a numerical instability which is characteristic to Roe-type scheme. Even though Roe-type numerical flux is less numerically dissipative and has good shock capturing ability, one problem arises which is a so-called "odd-even decoupling". This instability appears when the shock normal is directed parallel to the grid alignment. To avoid this instability, we adopt "carbuncle cure" in our NMHD code by following Hanawa et al. (2008).

3. GRMHD Code

Formalism of our GRMHD code is based mainly on Shibata & Sekiguchi (2005). It can be divided into two parts, one is MHD part and the other is Einstein's equation part. MHD part describes time evolution of matter on the background of spacetime metric and the metric is evolved according to Einstein's equation through the so-called "Baumgarte-Shapiro-Shibata-Nakamura (BSSN)" formalism (see, e.g., Shibata & Nakamura 1995; Baumgarte & Shapiro 1999; Yo et al. 2002).

Before going to brief summary of our method, we describe our fundamental variables of MHD and metric parts. We set fundamental variables of MHD part as rest-mass density ρ , specific internal energy ε , 4-velocity u^μ and magnetic field b^μ measured by a comoving observer. For metric part, the 3-metric γ_{ij} and the extrinsic curvature K_{ij} are the fundamental ones adopting the 3+1 formulation of "Arnowitt-Deser-Misner (ADM)" formalism (Arnowitt et al. 1962). Then the line element of the spacetime can be expressed as

$$ds^2 = -\alpha^2 dt^2 + \gamma_{ij}(dx^i + \beta^i dt)(dx^j + \beta^j dt) \quad (26)$$

Here α , β^i are the lapse function and the shift vector, respectively, and determined by arbitrary chosen gauge condition (Sec. 3.3). Hypersurface of constant t is foliated in the spacetime so that a unit normal vector $n^\mu(n_\mu)$ to this hypersurface becomes

$$n^\mu = (1, -\beta^i)/\alpha \quad \& \quad n_\mu = (-\alpha, 0) \quad (27)$$

Fundamental metrics γ_{ij} , K_{ij} are converted to 5 variables in BSSN formalism which are; the conformal exponent $\phi = \ln(\gamma)/12$, here γ is the determinant of 3-metric γ_{ij} ; the conformal 3-metric $\tilde{\gamma}_{ij} = e^{-4\phi}\gamma_{ij}$; the trace of the extrinsic curvature $K = \text{tr}(K_{ij})$; the tracefree extrinsic curvature $\tilde{A}_{ij} = e^{-4\phi}(K_{ij} - \gamma_{ij}K/3)$; and three auxiliary variables $F_i = \delta^{jk}\tilde{\gamma}_{ij,k}$, here " , k " represents partial derivative with respect to k direction. Hereafter, \tilde{D}_i and D_i denote the covariant derivatives with respect to $\tilde{\gamma}_{ij}$ and γ_{ij} , respectively.

Stress energy tensor for ideal magneto-hydrodynamical fluid is expressed as

$$T_{\mu\nu} = (\rho h + b^2)u_\mu u_\nu + (p + b^2/2)g_{\mu\nu} - b_\mu b_\nu \quad (28)$$

Here $h(= 1 + \varepsilon + p/\rho)$ is enthalpy and we define magnetic pressure as $b^2/2 = b^\mu b_\mu/2$. With these settings, we define other useful quantities which are; 3-velocity v^i observed by Eulerian observer at

rest; and magnetic field B^μ observed in the fluid frame, i.e., $u^\mu = n^\mu$.

$$v^i = u^i/u^t \quad (29)$$

$$B^\mu = (0, e^{6\phi}(Wb^i - \alpha b^t u^i)) \quad (30)$$

Here $W = \alpha u^t$ is the Lorentz factor. We also define primitive/conservative variables \mathbf{P}/\mathbf{Q} as

$$\mathbf{P} = (\rho, u_i, \varepsilon, B^i) \quad (31)$$

$$\mathbf{Q} = \begin{bmatrix} \rho_* \\ S_i \\ \tau \\ B^i \end{bmatrix} = \begin{bmatrix} \rho e^{6\phi} W \\ e^{6\phi}((\rho h + b^2)W u_i - \alpha b^t b_i) \\ e^{6\phi}((\rho h + b^2)W^2 - (p + b^2/2) - (\alpha b^t)^2) - \rho_* \\ B^i \end{bmatrix} \quad (32)$$

3.1. Magneto Hydrodynamical Equations

Basic equations of magneto-hydrodynamical part in general relativistic form are written as the following conservative-like equations.

$$\partial_t \rho_* + \partial_i(\rho_* v^i) = 0 \quad (33)$$

$$\begin{aligned} & \partial_t S_i + \partial_j(S_i v^j + \alpha e^{6\phi} P_{\text{tot}} \delta_i^j - B^j b_i/u^t) = \\ & -S_0 \partial_i \alpha + S_k \partial_i \beta^k + 2\alpha e^{6\phi} S_k^k \partial_i \phi - \alpha e^{2\phi} (S_{jk} - P_{\text{tot}} \gamma_{jk}) \partial_i \tilde{\gamma}^{jk}/2 \end{aligned} \quad (34)$$

$$\begin{aligned} & \partial_t \tau + \partial_i(S_0 v^i + e^{6\phi} P_{\text{tot}}(v^i + \beta^i) - \alpha b^t B^i/u^t - \rho_* v^i) = \\ & \alpha e^{6\phi} K S_k^k/3 + \alpha e^{2\phi} (S_{ij} - P_{\text{tot}} \gamma_{ij}) \tilde{A}^{ij} - S_i D^i \alpha \end{aligned} \quad (35)$$

$$\partial_t B^i + \partial_j(B^i v^j - v^i B^j) = 0 \quad (36)$$

Where $S_0 = \tau + \rho_*$ and these equations can be expressed in the form of $\partial_t \mathbf{Q} + \partial_i \mathbf{F}^i = \mathbf{S}$.

Our procedure to evolve the MHD conservative variables \mathbf{Q} is similar to our NMHD code except we use the HLL (Harten-Lax-van Leer) flux (Harten et al. 1983) and not Roe-type one. HLL-flux is less numerically expensive compared to Roe-flux, since we only have to consider the two fastest left and right going wave speed without considering eigenvectors like expressed in Eq. (8), however HLL-flux has sufficient capability to follow shocks and is suitable for our aims. The fastest left/right going wave speed are evaluated from 4th order eigenvalue problem (see, Eqs. (58), and (63-65), in Anton et al. 2006). We solve this problem by iterative Newton method with given sound speed. Following Shibata & Sekiguchi (2005), the sound speed a is defined as

$$a = \sqrt{\frac{1}{h} \left[\left. \frac{\partial P}{\partial \rho} \right|_\varepsilon + \frac{P}{\rho^2} \left. \frac{\partial P}{\partial \varepsilon} \right|_\rho \right]} \quad (37)$$

By solving 4th order eigenvalue problem the fastest left/right going wave speed λ_1/λ_7 (correspond to λ_1/λ_7 in Eq. (9)) can be obtained. We evaluate λ_1 and λ_7 at immediate left and right of the cell boundary by adopting several types of reconstruction schemes such as monotonized central (MC) or piecewise linear method (PLM). In this paper, we adopt only MC method which has second order convergence with respect to space. Then the fastest left/right going wave speed λ_-/λ_+ at cell boundary are defined as

$$\lambda_- = \max(0, \lambda_{1,L}, \lambda_{1,R}) \quad (38)$$

$$\lambda_+ = \max(0, \lambda_{7,L}, \lambda_{7,R}) \quad (39)$$

With these wave speed, we define HLL flux, by following Anton et al. (2006), as

$$\mathbf{F}_{HLL} = \frac{\tilde{\lambda}_+ \mathbf{F}(\mathbf{P}_L) - \tilde{\lambda}_- \mathbf{F}(\mathbf{P}_R) + \tilde{\lambda}_- \tilde{\lambda}_+ (\mathbf{Q}_R - \mathbf{Q}_L)}{\tilde{\lambda}_+ - \tilde{\lambda}_-} \quad (40)$$

Here $\tilde{\lambda} = \lambda/\alpha$ and $\mathbf{F}(\mathbf{P})$ is an appropriate flux vector in Eqs. (33-36). Solenoidal constraint of magnetic field is satisfied by CT scheme as the same procedure as NMHD.

Once we update conservative variables \mathbf{Q} , we have to obtain primitive variables \mathbf{P} by solving following three coupled equations with iterative Newton method.

$$\tau = \tau(\rho, \varepsilon, W) \quad (41)$$

$$S^i S_i = S^2(\rho, \varepsilon, W) \quad (42)$$

$$\rho_* = \rho_*(\rho, W) \quad (43)$$

We employ the same recovering procedure as proposed in Cerdá-Durán et al. (2008) with adopting "safe-guess values" when the iteration does not converge.

3.2. The BSSN Equations

Next we describe our method to evolve metric part. As previously mentioned we evolve BSSN variables $(\phi, \tilde{\gamma}_{ij}, K, \tilde{A}_{ij}, F_i)$ according to following equations (see, e.g., Shibata & Nakamura (1995); Baumgarte & Shapiro (1999); Yo et al. (2002)), .

$$(\partial_t - \mathcal{L}_\beta) \tilde{\gamma}_{ij} = -2\alpha \tilde{A}_{ij} \quad (44)$$

$$(\partial_t - \mathcal{L}_\beta) \phi = -\alpha K/6 \quad (45)$$

$$(\partial_t - \mathcal{L}_\beta) \tilde{A}_{ij} = e^{-4\phi} [\alpha(R_{ij} - 8\pi S_{ij}) - D_i D_j \alpha]^{\text{trf}} + \alpha(K \tilde{A}_{ij} - 2\tilde{A}_{ik} \tilde{\gamma}^{kl} \tilde{A}_{jl}) \quad (46)$$

$$(\partial_t - \mathcal{L}_\beta) K = -\Delta\alpha + \alpha(\tilde{A}_{ij} \tilde{A}^{ij} + K^2/3) + 4\pi\alpha(S_0 e^{-6\phi} + \gamma^{ij} S_{ij}) \quad (47)$$

$$\begin{aligned} (\partial_t - \beta^k \partial_k) F_i &= -16\pi\alpha e^{-6\phi} S_i \\ &+ 2\alpha \left[f^{jk} \tilde{A}_{ij,k} + f^{jk}{}_{,k} \tilde{A}_{ij} - \tilde{A}^{jk} h_{jk,i}/2 + 6\phi_{,j} \tilde{A}_i^j - 2K_{,i}/3 \right] \\ &+ \delta^{jk} \left[-2\alpha_{,k} \tilde{A}_{ij} + \beta^l{}_{,k} h_{ij,l} + (\tilde{\gamma}_{il} \beta^l{}_{,j} + \tilde{\gamma}_{jl} \beta^l{}_{,i} - 2\tilde{\gamma}_{ij} \beta^l{}_{,l}/3)_{,k} \right] \end{aligned} \quad (48)$$

In these Eqs. (44-48), \mathcal{L}_β is *Lie* derivative with respect to β^i ; "trf" denotes trace-free operator; $\Delta = D^i D_i$; $f^{ij} = \tilde{\gamma}^{ij} - \delta^{ij}$ and $h_{ij} = \tilde{\gamma}_{ij} - \delta_{ij}$. R_{ij} is the Ricci tensor and consisted of two parts in the form of

$$R_{ij} = \tilde{R}_{ij} + R_{ij}^\phi \quad (49)$$

For explicit forms of the Ricci tensor and several notes when calculating the Ricci scalar, see Shibata & Uryū (2002). We evolve these BSSN variables by the second order scheme in space (e.g., Appendix of Shibata 1999) and by the iterative Crank-Nicholson scheme with three steps in time. Many recent numerical simulations in full general relativity adopt fourth order scheme in space such as Zlochower et al. (2005) or Etienne et al. (2008). However, such higher order scheme is necessary especially when the metric is highly distorted such as around the BH. Our numerical simulations with a relatively low mass star ($15M_\odot$) do not show any BH formation and we thus consider second order scheme is acceptable at this time.

For the metric, there are several mathematical and physical constraints. As for the mathematical constraints, $\det(\tilde{\gamma}_{ij}) = 1$ and $\text{tr}(\tilde{A}_{ij}) = 0$ should be satisfied. We enforce following two artificial procedures

$$\tilde{\gamma}_{ij} \rightarrow \tilde{\gamma}_{ij} / \det(\tilde{\gamma}_{ij}) \quad (50)$$

$$\tilde{A}_{ij} \rightarrow \tilde{A}_{ij} - \tilde{\gamma}^{kl} \tilde{A}_{kl} \tilde{\gamma}_{ij} / 3 \quad (51)$$

after each update to maintain numerical stability. Physical constraints are the Hamiltonian and momentum constraints.

$$\mathcal{H} = \tilde{D}^i \tilde{D}_i e^\phi - \frac{e^\phi \tilde{R}}{8} + 2\pi S_0 e^{-\phi} + \frac{e^{5\phi}}{8} \left(\tilde{A}_{ij} \tilde{A}^{ij} - \frac{2}{3} K^2 \right) = 0 \quad (52)$$

$$\mathcal{M}_i = \tilde{D}_j \left(e^{6\phi} \tilde{A}^j_i \right) - \frac{2}{3} e^{6\phi} \tilde{D}_i K - 8\pi S_i = 0 \quad (53)$$

We do not enforce any artificial modifications to satisfy these constraints, though monitor these values just as our code check. However, we enforce Hamiltonian constraint every time we refine/coarsen the AMR blocks by solving above Poisson like non-linear equation(52). We monitor $C_{\mathcal{H}}$ defined by

$$C_{\mathcal{H}} = \frac{1}{M_{\text{bar}}} \int \frac{\rho_* \mathcal{H}}{\left[|\tilde{D}^i \tilde{D}_i e^\phi| + \left| \frac{e^\phi \tilde{R}}{8} \right| + |2\pi S_0 e^{-\phi}| + \left| \frac{e^{5\phi}}{8} \left(\tilde{A}_{ij} \tilde{A}^{ij} - \frac{2}{3} K^2 \right) \right| \right]} dx^3 \quad (54)$$

to check the Hamiltonian constraint and accuracy of our code. Here, M_{bar} is proper rest mass and defined by Eq. (57).

3.3. Gauge Conditions

Hyper-surface at constant time t can be foliated in spacetime arbitrary, but is usually chosen so as to keep time evolution numerically most stable. As for the time slicing condition which determines lapse (α), we adopt several choices in our GRMHD code such as "the approximate maximal

slicing” or ”harmonic slicing” or ”1+log” slicing conditions. Since the approximate maximal slicing condition requires to solve poisson like non-linear equation every time step and very time consuming method, we usually adopt 1+log gauge condition given by

$$\partial_t \alpha = \beta^i \partial_i \alpha - 2\alpha K \quad (55)$$

We have implemented ”dynamical gauge condition” for shift (β^i), following Shibata (2003), which is given by solving

$$\partial_t \beta^i = \tilde{\gamma}^{ij} (F_j + \Delta t \partial_t F_j) \quad (56)$$

Where, Δt is the numerical time step. By imposing these gauge conditions, we do not suffer from time consuming Poisson like equations at every time step, while we do not encounter any numerical instabilities throughout our calculations of core collapse of massive star.

3.4. Diagnostics in GRMHD

In GRMHD code, global quantities such as total baryon rest mass M_{bar} ; ADM mass M_{ADM} ; total angular momentum along the rotational (z) axis J_z ; internal energy E_{int} ; magnetic energy E_{mag} ; kinetic energy T_{kin} ; rotational kinetic energy T_{rot} are defined as expressed below (see, e.g., Duez et al. 2003; Kiuchi et al. 2008).

$$M_{\text{bar}} = \int \rho_* dx^3 \quad (57)$$

$$M_{\text{ADM}} = \int \left[S_0 e^{-\phi} + \frac{e^{5\phi}}{16\pi} \left(\tilde{A}_{ij} \tilde{A}^{ij} - \frac{2}{3} K^2 - \tilde{\gamma}^{ij} \tilde{R}_{ij} e^{-4\phi} \right) \right] dx^3 \quad (58)$$

$$J_z = \int \left[\frac{\tilde{A}_y^x - \tilde{A}_x^y}{8\pi} + x S_y - y S_x + \frac{x K_{,y} - y K_{,x}}{12\pi} - \frac{x \tilde{\gamma}_{,y}^{ij} \tilde{A}_{ij} - y \tilde{\gamma}_{,x}^{ij} \tilde{A}_{ij}}{16\pi} \right] e^{6\phi} dx^3 \quad (59)$$

$$E_{\text{int}} = \int \rho_* \varepsilon dx^3 \quad (60)$$

$$T_{\text{kin}} = \int \rho_* h u_i v^i dx^3 \quad (61)$$

$$T_{\text{rot}} = \int \rho_* h u_\phi v^\phi dx^3 \quad (62)$$

$$E_{\text{mag}} = \int \frac{b^2}{2} W e^{6\phi} dx^3 \quad (63)$$

Then the gravitational potential energy E_{grv} is defined by $E_{\text{grv}} = -(M_{\text{bar}} - M_{\text{ADM}} + E_{\text{int}} + T_{\text{kin}} + E_{\text{mag}})$. Because of our formulae for MHD part and because of our AMR scheme (see, Sec. 4.3), M_{bar} is conserved with high accuracy. On the other hand, conservation of M_{ADM} which is guaranteed from the Einstein’s equation in the absence of gravitational radiation is violated due to the accumulation of numerical errors in our CCSNe simulations. Then, several % fluctuation appears (see, Fig.16 in Sec. 6) which is approximately 2-3 orders larger compared to that of M_{bar}

in our CCSNe simulations. Consequently even though our initial condition satisfies $E_{\text{grv}} < 0$ (i.e., gravitationally trapped system), there sometimes appear that $E_{\text{grv}} > 0$ during calculation. Therefore we estimate the gravitational potential energy as $E_{\text{grv}} \sim -(E_{\text{int}} + T_{\text{kin}} + E_{\text{mag}})$ and apply it to such as the rotational to gravitational energy $\beta_{\text{rot}} = T_{\text{rot}}/|E_{\text{grv}}|$.

4. Adaptive Mesh Refinement

One of difficulties in computational astrophysics is that we have to handle wide dynamical range in a limited computational resource. For instance, in the context of CCSN simulation, the PNS is a size of ~ 10 km and on the other hand radius of the iron core is the order of $\gtrsim O(1000)$ km. If we cover such a vast range (several times of the iron core) with a uniform resolution, e.g., ~ 500 m to resolve interior of the PNS, it becomes impossible to calculate with our limited computational resource. We thus raise resolution in the vicinity of proto-neutronstar and, at the same time, lower resolution far from the centre. To realize such situation, we incorporate the AMR technique (e.g., Berger & Colella 1989; Powell et al. 1999) into our codes.

4.1. AMR Structure

In our codes, computational domain is divided into "blocks" (hereafter, AMR block) and every AMR block consists of $8 \times 8 \times 8$ cubic cells and of 2 additional cells as ghost zones in every side of block. Every AMR block belongs to a refinement level " l " and if the refinement level l is raised by one, the AMR block is divided into 8 blocks with halved cell width. On the other hand, if all $2 \times 2 \times 2$ neighboring AMR blocks are assigned to lower their refinement level by one, 8 blocks merge into one block with twice cell width.

Our codes are fully parallelized and adopt Message Passing Interface (MPI) for communication between different nodes. Then it requires load balancing in AMR frame work. Our method for this purpose is like this. Three dimensional structure of AMR blocks are projected on one dimensional structure connected by "Hilbert" space filling curve (Hilbert 1891). Along the *Hilbert* curve, AMR blocks are numbered sequentially. Then AMR blocks projected on one dimension are allocated to all computational nodes in a straight forward manner. Using such a projection scheme, e.g., connecting by *Hilbert* curve, enables us to minimize the data transfer between different computational nodes. This is because surface area of a "chunk" of AMR blocks allocated in one node by above method is minimized as much as possible and, thus, we can minimize time to spare for the data communication. In *top-left* panel of Fig.2, we display an example of *Hilbert* curve in two dimension. In this figure, asterisks(circles, crosses) denote centers of cells with width 0.5(0.25, 0.125) and lines are *Hilbert* curves. As seen in this panel, two dimensional structure of AMR blocks is projected on one dimension. In *right-top* panel, we again display *Hilbert* curve which fills two dimensional computational domain covered by blocks of four different AMR levels. Background colors represent

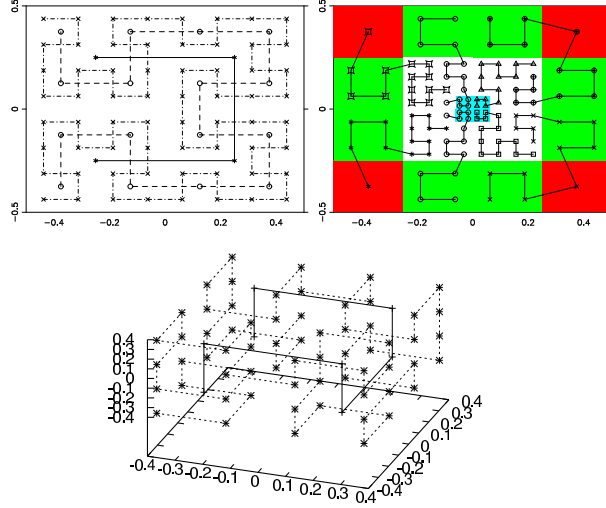


Fig. 2.— *Top-left*: Hilbert curves filling two dimensional area covered by uniform AMR blocks with three different levels. *Top-right*: Hilbert curves filling two dimensional area covered by nonuniform AMR blocks with four different AMR levels. In this panel, AMR blocks are allocated to 8 nodes and blocks allocated to one node are connected through one sequential line. *Bottom*: Three dimensional extension of *top-left* panel with two different levels.

AMR levels and blocks connected one curve are allocated to one computational node. Therefore, in this panel, all AMR blocks are allocated to 8 nodes with maintaining load balancing. In *bottom* panel, we also display three dimensional extension of Hilbert curves with two different AMR levels for reference.

By adopting such method, our AMR structure has flexibility to refine or coarsen AMR blocks locally.

4.2. Poisson Solver under the AMR Framework

In NMHD code, we have to solve Poisson equation in the form of $Ax = B$ for the self gravity and; in GRMHD code, Poisson like non linear equation in the form of $Ax = B(x)$ for the initial Hamiltonian and momentum constraints. Here A is a given $(N_{\text{block}} \times 8 \times 8 \times 8) \times (N_{\text{block}} \times 8 \times 8 \times 8)$ matrix, B is a given $(N_{\text{block}} \times 8 \times 8 \times 8)$ vector and x is a solution we seek which is $(N_{\text{block}} \times 8 \times 8 \times 8)$ vector. N_{block} is a total number of AMR blocks. In GRMHD, $B(x)$ is a vector containing non-linear term of x . We adopt iterating method, the so called "BiConjugate Gradient Stabilized (BiCGSTAB)" (van der Vorst 1992) method to solve such huge simultaneous equations. Our strategy for solving this equation under our AMR structure is; (1) we set an AMR level l which is 0 at initial; (2) for all AMR boxes whose AMR levels are larger or equal to l , we project their physical quantities, such as the density, to boxes of AMR level l by the coarsening

procedure and construct A & B ; (3) we then solve equation by BiCGSTAB on the uniform mesh with appropriate boundary conditions at the interface of AMR level l and $l - 1$ and also at the outer boundary; (4) increment l by one and repeat these procedures from (1) again. Note that, we have to pay special attention at the interface of different AMR level, i.e., l and $l - 1$. At here, we have to connect both the solutions and their first derivation smoothly, otherwise there appear some non-physical divergence. To avoid this, we adopt quadratic and bilinear interpolation methods following Matsumoto (2007) to evaluate ghost zone values of AMR level l , e.g., $\Phi(i - 1, j)$ and $\Phi(i - 2, j)$ in Fig.3. Here, we summarize our interpolation method in two dimension. Three dimensional extension can be done in a straightforward manner. If we seek gravitational potential $\Phi(i - 1, j)$, we first have to obtain $\Phi(A)$ at $(I, J - 1/4)$ which is derived via

$$\Phi(A) = \Phi(I, J) - \frac{1}{2}\text{MC}(\Phi(I, J + 1) - \Phi(I, J), \Phi(I, J) - \Phi(I, J - 1)) \quad (64)$$

Here, $\text{MC}(x, y)$ is the monotonized central method. Then $\Phi(i - 1, j)$ is derived via quadratic

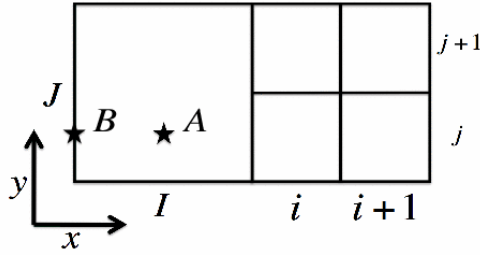


Fig. 3.— Schematic figure of interpolation of ghost zone value. Four small boxes and one large box belong to AMR level l and $l - 1$, respectively.

interpolation

$$\Phi(i - 1, j) = \frac{10\Phi(i, j) - 8\Phi(A) + 3\Phi(i + 1, j)}{15} \quad (65)$$

$\Phi(B)$ which is required to evaluate $\Phi(i - 2, j)$ is obtained by following equation

$$\Phi(B) = \frac{\Phi(I, J) + \Phi(I - 1, J)}{2} - \frac{1}{2}\text{MC}\left(\frac{\Phi(I, J + 1) + \Phi(I - 1, J + 1)}{2} - \frac{\Phi(I, J) + \Phi(I - 1, J)}{2}, \frac{\Phi(I, J) + \Phi(I - 1, J)}{2} - \frac{\Phi(I, J - 1) + \Phi(I - 1, J - 1)}{2}\right) \quad (66)$$

Three dimensional extension of this smoothening method is done by replacing, e.g, Eq.(64), with bilinear interpolation

$$\begin{aligned} \Phi(A) = \Phi(I, J, K) & - \frac{1}{2}\text{MC}(\Phi(I, J + 1, K) - \Phi(I, J, K), \Phi(I, J, K) - \Phi(I, J - 1, K)) \\ & - \frac{1}{2}\text{MC}(\Phi(I, J, K + 1) - \Phi(I, J, K), \Phi(I, J, K) - \Phi(I, J, K - 1)) \end{aligned} \quad (67)$$

On the other hand, lower level ghost zone value $\Phi(I + 1, J)$ is derived by "*restriction*" procedure and this is simply averaging Φ over the 2×2 (or $2 \times 2 \times 2$ in 3D) adjacent cells via

$$\Phi(I + 1, J) = \frac{1}{4} \sum_{n,m=0,1} \Phi(i + n, j + m) \quad (68)$$

4.3. Boundary of AMR Blocks

To guarantee the conservation law and the solenoidal constraint of magnetic field, we have to reflux the numerical flux, Eqs. (8) and (40), and the electric field, Eq.(25), at where AMR boxes of different levels are contacting. In Fig.4, we display schematic picture of refluxing procedures. For instance, the numerical flux F_x belonging to AMR level $l - 1$ and defined at cell boundary is replaced by summation of $f_{x,i}$ ($i = 1, 2, 3, 4$) which belong to AMR level l . Similarly, as for the electric field, the electric field E_y defined at cell edge is replaced by summation of $e_{y,i}$ ($i = 1, 2$). These procedures ensure the conservation and the solenoidal constraint below the round off error.

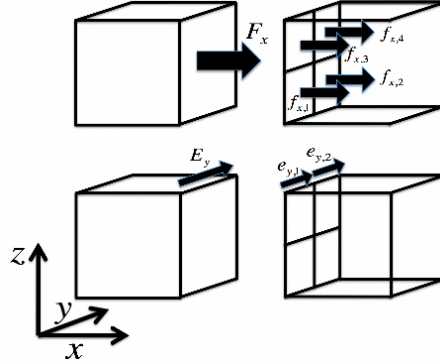


Fig. 4.— Schematic picture of refluxing of the numerical flux $F_x(f_x)$ and the electric field $E_y(e_y)$. Left two and right boxes belong to AMR level $l - 1$ and l , respectively.

Additionally, as for the ghost zones, we have to obtain physical variables every after the time updating and this procedure is sorted into three cases.

(1) For AMR box whose neighbor has the same AMR level, we simply copy all physical variables.

(2) For AMR box whose neighbor has lower level, ghost zone variables are interpolated and are sent from lower to higher level box. For this interpolation, we use the same method as used in our Poisson solver (described in Sec. 4.2) other than the magnetic field \mathbf{B} . As for the magnetic field, we have to interpolate while maintaining the solenoidal constraint and this is done by adopting the same method proposed by Balsara (2001).

(3) If AMR level of the neighbor is higher, physical variables are evaluated by "*restriction*"

procedure. In our codes, this restriction procedure is simply averaging the variables of $2 \times 2 \times 2$ adjacent cells which is the same method as used in our Poisson solver (Sec. 4.2).

4.4. The BSSN Evolution Under the AMR Framework

During time evolution of the BSSN variables, we have to derive the spatial derivatives of metrics not only along one direction, e.g., ∂_x , but also the cross derivatives, e.g., ∂_{xy} to obtain such as the Ricci tensor. Therefore, if there exist some discontinuity in the spatial derivatives across the AMR refinement boundary, spurious oscillations of the BSSN variables appear near the refinement boundary. Since the time marching is simultaneous across all the AMR boxes in our codes, there is no time lag between different AMR levels. However, we should carefully interpolate the buffer zone’s metrics especially for AMR boxes whose neighbors have lower AMR levels than theirs. This situation is the same as that appeared in our Poisson solver (Sec. 4.2) and we adopt the same strategy to obtain the buffer zone’s variables. In addition we have to evaluate the metrics along the edge of AMR block (e.g., $(i, j, k) = (9, 9, 1 \sim 8)$) for the cross derivatives and this evaluation can be done in a similar manner as that in the normal buffer zone’s case. For instance, if we seek a metric X at $(i, j, k) = (9, 9, 1)$, $X(A)$ which corresponds to $\Phi(A)$ in Eq. (64) is replaced by

$$X(A) = X(1, 1, 1) - \frac{1}{2}MC(X(1, 1, 2) - X(1, 1, 1), X(1, 1, 1) - X(1, 1, 0)) \quad (69)$$

Then, in a straight forward manner of Eq. (65), $X(9, 9, 1)$ can be derived by

$$X(9, 9, 1) = \frac{10X(8, 8, 1) - 8X(A) + 3X(7, 7, 1)}{15} \quad (70)$$

However, we cannot completely suppress the spurious oscillations in the refinement boundary and, in such case, adding numerical dissipation is sometimes useful (Schnetter et al. 2004). Even though we do not add the dissipation at present codes, we do not suffer from growth of the noises and the code crash. Several tests of the BSSN evolution with AMR structure are summarized in Sec.6.4.

5. Tests for NMHD Code

In this section, we introduce several test problems done by our newly developed 3DMHD code in the Newtonian approximation. We verified the accuracies of our new AMR-NMHD code through several test suites.

5.1. One Dimensional Shock Tube Test

We calculated several 1-D hydrodynamical shock tube tests and compared to the exact solutions obtained from the code HE-E1RPEXACT of the library *NUMERICA* (Toro 1999). We show one test in Fig.5 in which we assumed ideal gas with adiabatic index $\gamma = 1.4$. The mesh width of exact solution is 1/1000, meanwhile, the "effective" mesh width of our numerical run's are 1/2048, 1/512, 1/128 for *blue*, *green* and *red* dots, respectively.

test 1)

$$(\rho, V_x, P_{\text{tot}}) = \begin{cases} (1.0, 0.0, 1000.0) & x \leq 0.5 \\ (1.0, 0.0, 0.01) & x > 0.5 \end{cases}$$

For MHD shock tube test, we show the same test described in (Brio & Wu 1988) with three

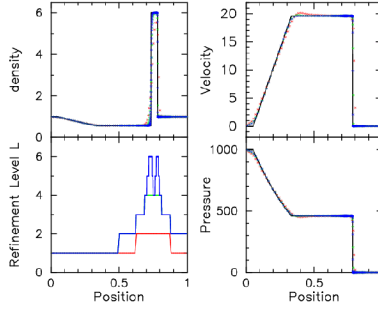


Fig. 5.— Results of test 1) at $t = 0.012$. *Black* solid line is analytical solution and *blue*, *green* and *red* dots/lines are our numerical results. Each color represents the maximum refinement level $L_{\text{AMR,max}}$. We set $L_{\text{AMR,max}} = 2, 4, 6$ for *red*, *green* and *blue*, respectively.

different types of the EOSs in Fig.6.

test 2)

$$(\rho, \mathbf{V}, B_x, B_y, B_z, P_{\text{tot}}) = \begin{cases} (1.0, \mathbf{0}, 0.75\sqrt{4\pi}, \sqrt{4\pi}, 0.0, 1.0) & x \leq 0.5 \\ (0.125, \mathbf{0}, 0.75\sqrt{4\pi}, -\sqrt{4\pi}, 0.0, 0.1) & x > 0.5 \end{cases}$$

Initial total pressure P_{tot} , which excludes the magnetic pressure, is divided into three parts such as the gas (P_{gas}), the degenerate (P_{dege}) and the radiation (P_{rad}) pressure term.

$$\begin{aligned} a) : P_{\text{tot}} &= P_{\text{gas}} = \rho T \\ b) : P_{\text{tot}} &= P_{\text{gas}} + P_{\text{dege}} = \rho T + 0.3\rho^{4/3} \\ c) : P_{\text{tot}} &= P_{\text{gas}} + P_{\text{dege}} + P_{\text{rad}} = \rho T + 0.3\rho^{4/3} + T^4/3 \end{aligned}$$

Internal energy has also three parts corresponding to the gas (ε_{gas}), the Fermi ($\varepsilon_{\text{dege}}$) and the radiation (ε_{rad}) energy as defined by the following.

$$\varepsilon_{\text{tot}}(\rho, T) = \varepsilon_{\text{gas}} + \varepsilon_{\text{dege}} + \varepsilon_{\text{rad}}$$

$$= \frac{P_{gas}}{(\gamma - 1)\rho} + \int_0^\rho \frac{P_{dege}}{\rho^2} d\rho + \frac{3P_{rad}}{\rho}$$

Here $\gamma = 2.0$ and EOS a) corresponds to the original model reported in Brio & Wu (1988). From

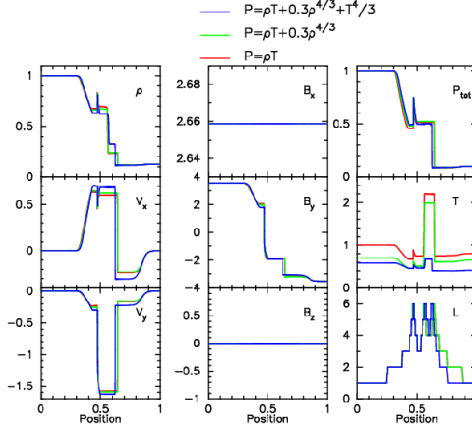


Fig. 6.— Results of test 2) at $t = 0.1$. Each line corresponds to different EOS shown at the top.

Fig.5-6, we see that our code captures the discontinuities accurately and also no numerical instabilities are seen.

5.2. Poisson Solver

As for the tests of our Poisson solver, we set two types of spherically symmetric density distribution like below which have analytical solutions and compare our results with analytical ones.

- test 3) Homogeneous sphere of radius R and density ρ_0
- test 4) Centrally condensed sphere with density distribution $\rho(r)$

$$\rho(r) = \begin{cases} \frac{\rho_0}{1+(r/r_c)^2} & r < R \\ 0 & r > R \end{cases} \quad (71)$$

These tests are the same tests done in Stone & Norman (1992) and have analytical solutions, thus we can easily check the accuracy of our Poisson solver (for analytical formulae, see Stone & Norman 1992). We set $R = 10^8 \text{cm}$, $\rho_0 = 10^{12} \text{g cm}^{-3}$ and $r_c = 3 \times 10^7 \text{cm}$ for both tests 3) & 4). Fig.7 shows our numerical results with comparing analytical ones. *Upper* and *lower* two panels show $|d\nabla\phi| \equiv |(\nabla\phi_{\text{ana}} - \nabla\phi)/\nabla\phi_{\text{ana}}|$ and $|d\phi| \equiv |(\phi_{\text{ana}} - \phi)/\phi_{\text{ana}}|$, respectively. Here, ϕ is the numerical result of the Poisson equation and ϕ_{ana} is the analytical one. Deviations of our numerical results from the analytical ones are $\sim 0.1\%$ and we also find neither kink nor jump of both ϕ and $\nabla\phi$ at the interface of different AMR level boxes. Therefore, we consider our Poisson solver under AMR structure works with sufficient accuracy.

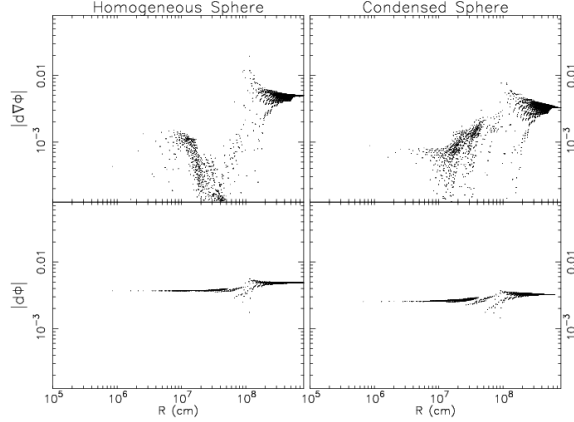


Fig. 7.— Results of test 3) (*left*) and 4) (*right*). See text for the definitions of $|d\phi|$ and $|d\nabla\phi|$. Five different levels of AMR boxes are drawn.

5.3. Energy and Angular Momentum Conservations

In this subsection, we check our NMHD code’s accuracy against the energy and the angular momentum conservations. Since we consider one of energy source of the formation of bipolar outflow is the extracted angular momentum, we have to carefully trace the time evolution of angular momentum. As for the test of angular momentum transfer, we follow the collapse of a non-magnetized and rotating $25M_{\odot}$ star with the adiabatic gas with index $\gamma = 1.4$. If no magnetic field exists and the fluid is adiabatic gas, the angular momentum is not transported. Result is shown in Fig.8. Abscissa and vertical axes represent the specific angular momentum and the total mass in solar mass unit which is the summation of fluid elements having less or equal to the corresponding specific angular momentum on the abscissa axis, respectively. If the angular momentum conservation is maintained, the curves do not change its form in time and we thus see the angular momentum conservation is well maintained from this figure. As for the energy conservation test, we calculate collapse of a rotating and magnetized $15M_{\odot}$ star (corresponds to model “NB12R020Sf” described later in Sec.7). In Fig.9, we display time evolutions of various energy components and the error in energy conservation in *left* panel and the magnified view around the time of core bounce with different numerical resolutions to see the numerical convergence in *right* panel. As for the numerical convergence test, the computational domain is chosen as $(x, y, z) = [-5000, 5000]$ km for *solid* curves and $(x, y, z) = [-4000, 4000]$ km for *dashed* ones. Then the minimum grid widths become $\Delta x_{\min} = 600$ (*solid*) and 480 (*dashed*) m. From Fig.9, we see the energy conservation is well maintained and also see the numerical convergence is achieved within the range of our adopted numerical resolutions.

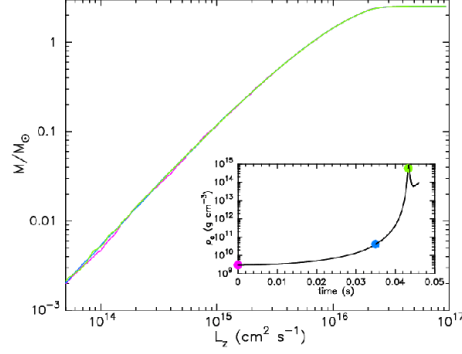


Fig. 8.— The angular momentum conservation. Abscissa and vertical axes represent the specific angular momentum and the total mass in solar mass unit which is the summation of fluid elements having less or equal to the corresponding specific angular momentum on the abscissa axis, respectively. In the inner mini-panel, the time evolution of the central density is displayed. Each Color of line represents the elapsed time from the initiation of collapse and corresponds to the same color-coded circle in the mini-panel.

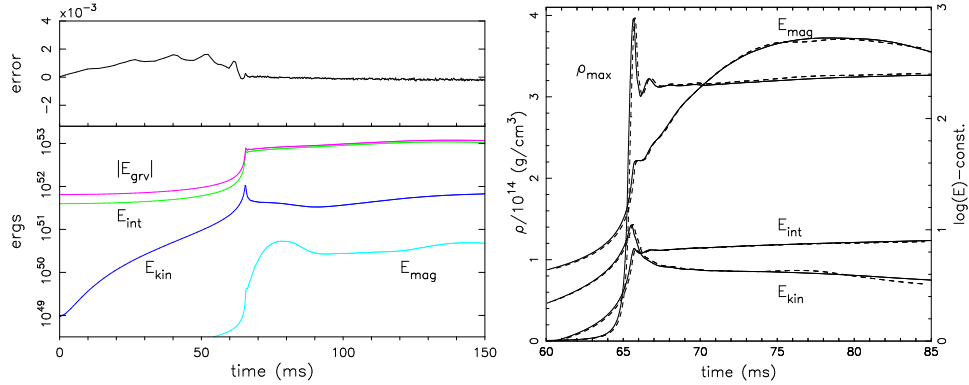


Fig. 9.— *Left*: The error in energy conservation and time evolutions of various energy components. E_{grv} , E_{int} , E_{kin} and E_{mag} represent gravitational, internal, kinetic and magnetic energy, respectively. Relative error is defined by a deviation of $(E_{\text{grv}} + E_{\text{int}} + E_{\text{kin}} + E_{\text{mag}})/|E_{\text{grv}}|$ from its initial value and is shown in upper part. Energy conservation is maintained within $\sim 0.2\%$ error through our time evolution. *Right*: Magnified view around the time of core bounce to see the numerical convergence with respect to the grid resolution. *Solid* and *dashed* curves correspond to models with minimum resolution $\Delta x_{\text{min}} = 600\text{m}$ and $\Delta x_{\text{min}} = 480\text{m}$, respectively. The internal, kinetic and magnetic energies are normalized by 10^{52} , 10^{51} and 10^{48} , respectively.

6. Tests for GRMHD Code

In this section, we introduce several test problems done by our newly developed 3DGRMHD code.

6.1. One Dimensional Shock Tube Test

As for the basic test, we calculated the relativistic Brio & Wu MHD shock tube test (see, Brio & Wu 1988; Komissarov 1999) with fixed flat metric and the results are shown in Fig.10. In

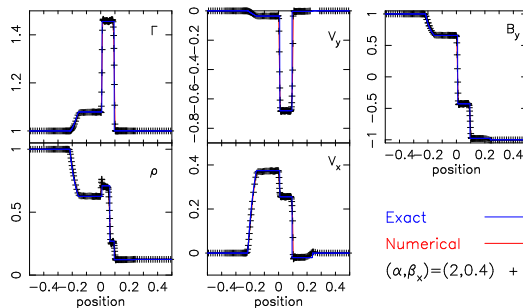


Fig. 10.— The relativistic version of Brio & Wu MHD shock tube test. Exact solutions are obtained from Giacomazzo & Rezzolla (2006) and drawn with blue lines. Γ is the Lorentz factor and other notations are the same as in Fig.6. Numerical results (*red* lines) are models with the gauge condition $(\alpha, \beta_x) = (1.0, 0.0)$ and black crosses are the one with $(\alpha, \beta_x) = (2.0, 0.4)$. Levels of AMR blocks are from 0 to 3 and the highest resolution is $\Delta x = 1/512$. Time slice is chosen at $t = 0.25$ for $\alpha = 1$ models and $t = 0.125$ for $\alpha = 2$ model. Results are shifted to $x \rightarrow x + 0.4 \times t$ for non-zero shift gauge model.

this figure, we show two models with different gauge conditions and compare with the exact solutions obtained from Giacomazzo & Rezzolla (2006). One is $(\alpha, \beta_x) = (1.0, 0.0)$ and represented by *red* lines and the other is $(\alpha, \beta_x) = (2.0, 0.4)$ and plotted by crosses. Time slice is taken at $t = 0.25$ and $t = 0.125$ for $\alpha = 1$ and 2, respectively. In addition, for non-zero shift gauge ($\beta_x = 0.4$) model, results are shifted to $x \rightarrow x + 0.4 \times t$ to let it coincides with other results. We can see our GRMHD code can handle the non-zero gauge conditions and shocks.

6.2. Bondi Accretion

In this subsection, we test our GRMHD code in a strongly curved and fixed spacetime. As for the test, we evolve the Bondi accretion flow with/without magnetic field and compare our results to analytical solution which are obtained according to Hawley et al. (1984). It is known that the radial magnetic field does not influence the Bondi accretion (De Villiers & Hawley 2003) and, thus,

we add the initial magnetic field via

$$\mathbf{B} = \nabla \times \left[\frac{B_0}{r(r+z)} (-y, x, 0) \right] \quad (72)$$

In this test, we adopt Kerr-Schild coordinate

$$\alpha = \frac{1}{\sqrt{1+2/r}} \quad (73)$$

$$\beta^i = \left(\frac{2}{2+r} \right) \frac{x^i}{r} \quad (74)$$

$$\gamma_{ii} = (1+2/r, r^2, r^2 \sin^2 \theta) \quad (75)$$

Here, the metric γ_{ii} is written in spherical polar coordinate. Event horizon locates $r = 2$ and outer boundary is set at $|x, y, z| = 10$. We excise the computational domain $|x, y, z| \leq 1.5$ and simply connect the non- and excised region with first order extrapolation. We run four models with two different resolutions ($N_{\text{block}} = 8^3, 16^3$) and $B_{\text{Horizon}}^r = 1$ (or $b^2/\rho|_{\text{Horizon}} = 2.446$) and $B_{\text{Horizon}}^r = 0$. In Fig.11, we show the rest density profiles of magnetized models at $t = 100M$ in *left* panel and L2 norm of the errors in density in *right* panel. The errors in $N_{\text{block}} = 8^3$ models are multiplied by $(1/2)^2$ to show the second order convergence. From this test, we see that our GRMHD code which employs HLL flux with MC limiter actually reproduces the second order convergence and also that our code can treat the strongly curved spacetime.

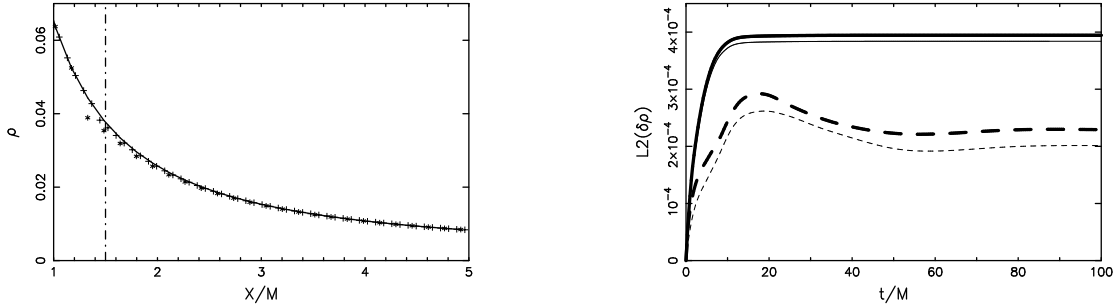


Fig. 11.— *Left*: Density plots of magnetized Bondi accretion test with different resolutions taken at $t = 100M$. *Solid* line represents analytical solution and the vertical *dash-dotted* line is where we excise the computational domain. *Asterisks* and *crosses* represent our results with different numerical resolutions. They correspond to $N_{\text{block}} = 16^3$ (*Asterisk*) and $N_{\text{block}} = 8^3$ (*cross*), respectively. *Right*: L2 norms of the errors in density from analytical value. *Long-dashed* lines are non magnetized accretion models and *solid* lines are magnetized models with $B^r|_{\text{Horizon}} = 1.0$ (or $b^2/\rho|_{\text{Horizon}} = 2.446$). Thick lines are $N_{\text{block}} = 8^3$ models, while thin lines are $N_{\text{block}} = 16^3$ models. Note that the errors of $N_{\text{block}} = 8^3$ models are multiplied by $(1/2)^2$ to show the second order convergence.

6.3. $\text{div}(\mathbf{B}) = 0$ Constraint

To check whether our two codes satisfy the solenoidal constraint for the magnetic field, we have checked the value $\text{div}(\mathbf{B})/B$. Fig.12 display $\text{div}(\mathbf{B})/B$ in the central $[0, 100] \times [0, 100] \times [0, 100]\text{km}^3$ region from one representative model of GRMHD models. In this region, three different AMR level boxes exist. At this moment, it almost reaches core bounce time and three times refinement procedures have been done since the initiation of calculation. From this figure, we see that solenoidal constraint is well maintained below the round-off error which tells us that both the refinement procedures and the electric field refluxing work well.

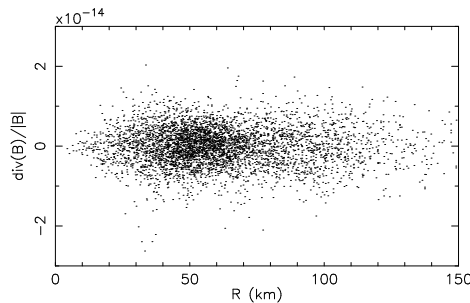


Fig. 12.— $\text{div}(\mathbf{B})/B$ is plotted of model "GB12R020Sf". In this figure, three different AMR levels are plotted in the central $[0, 100] \times [0, 100] \times [0, 100]\text{km}^3$ region.

6.4. Test Problems With Dynamical Background

In this subsection, we test our dynamical metric solver written by the BSSN formalism with and without matters.

6.4.1. Linearized Teukolsky Wave

First test is to follow the linearized gravitational waves, the so called "Teukolsky wave" (Teukolsky 1982), in a vacuum space. Following Shibata & Nakamura (1995), we adopt the same mode $l = |m| = 2$ and the initial wave amplitude is set to $C = 0.01$. For time slicing gauge condition, we adopt "1 + log" condition (see, Sec. 3.3). In this test, we also check the influence of the boundary where different AMR level boxes are contacting. In Fig.13, the initial condition (a component of the extrinsic curvature, K_{12}) and AMR structure are displayed. As seen in this figure, the inner region of $|x, y, z| \leq 5$ is covered by maximum AMR level meshes which we vary as $L_{\text{AMR}} = 1, 2$ and 3 to see convergence of the error. We extract the metric variables γ_{yy} and γ_{zz} at $(x, y, z) = (4.2, 0, 0)$ and compared them with analytical ones in Fig.14. *Red* curves are analytical solutions (see, e.g., Nakamura et al. (1987)) and *black* curves are numerical results. Numerical

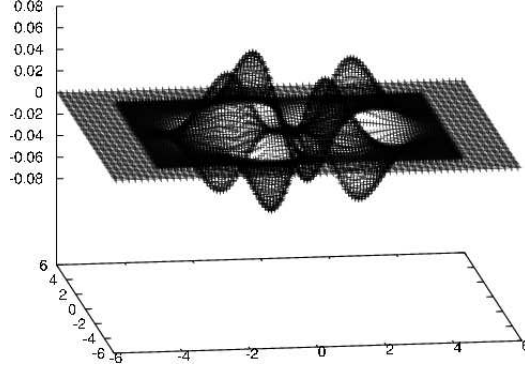


Fig. 13.— Our AMR structure and initial value of the extrinsic curvature K_{12} in the equatorial plane of linearized "Teukolsky wave test". The inner region of $|x, y, z| \lesssim 5$ is covered by higher resolution meshes.

resolutions are $\Delta x_{\min} = 0.078$ (*solid*), 0.156 (*dash-dotted*) and 0.312 (*dashed*). From *top* panel of Fig.14, we see that the errors decrease with increasing numerical resolution.

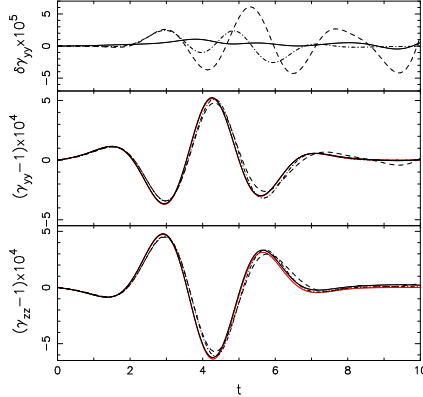


Fig. 14.— Results of linearized "Teukolsky wave test". *Bottom* and *middle* panels represent $\gamma_{zz} - 1$ and $\gamma_{yy} - 1$, extracted at $(x, y, z) = (4.2, 0, 0)$, respectively. *Red* lines are analytical solutions and *solid*, *dash-dotted* and *dashed* lines are results of maximum AMR level 3, 2 and 1, respectively. In model with maximum AMR level 3, the minimum grid resolution is $\Delta x_{\min} = 0.078$. *Top* panel represents deviations of γ_{yy} from analytical value with three different grid resolutions.

6.4.2. Rotating Neutron Star

Next test is an evolution of rigidly rotating neutronstar in equilibrium state. Initial parameters are the central rest density $\rho_c = 10^{-3}$ and the central angular velocity $\Omega_c = 10^{-2}$. We use the

polytropic EOS $P = K\rho^\Gamma$ where $K = 10$ and $\Gamma = 5/3$ and assume rigid rotation. With these parameters, the central lapse is $\alpha = 0.701$ and the ADM/baryon masses are $M_{\text{ADM}} = 1.49/M_{\text{bar}} = 1.55$. Outer boundary is taken at $|x, y, z| = L_{\text{out}} = 17$ and the equatorial radius of the NS is ~ 13.1 . In Fig.15, we display 4 models with two different numerical resolutions $\Delta x_{\text{min}} = L_{\text{out}}/32$ (models A and C), $\Delta x_{\text{min}} = L_{\text{out}}/64$ (models B and D). Models C and D are evolved with fixed matter distribution and only metrics are evolved, while, in models A and B, both matters and metrics are evolved. *Upper* and *lower* panels display time evolutions of deviations of the central lapse and the ADM mass from their initial values, respectively. In the *lower* panel, we also display the time evolutions of baryon mass for models A and B with thick lines. From this figure, we see that models C and D keep their initial configurations within 1%, while fully evolved models A and B show gradual decrease(increase) of ADM mass(central lapse). In this test, our treatment of the low density region outside of the NS is like this. We set the floor density value as $\rho_{\text{floor}} = 10^{-9} \times \rho_{c,\text{max}}$ and, in every time step, for all cells whose density is smaller than $10 \times \rho_{\text{floor}}$, we assume them as vacuum. Then their density and velocity are reset to ρ_{floor} and 0, respectively. We consider that this treatment is too simple and, e.g., the conservation of baryon mass is violated as seen in thick lines. However, in the context of CCSNe, we currently do not have to treat vacuum space and, additionally, models A and B show numerical convergence with respect to grid resolution, we consider our GR code works with sufficient level for our aims.

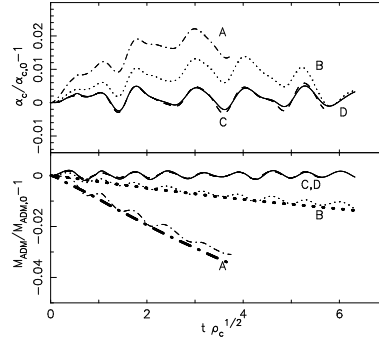


Fig. 15.— Time evolutions of the central lapse (*top*) and the ADM mass (*bottom*) normalized by their initial values. A (*dash-dotted*) and B (*dotted*) are fully (both matters and metrics) evolved models, while, in C (*dash*) and D (*solid*), only metrics are evolved. In the *bottom* panel, we also plot the time evolutions of baryon mass with thick lines. Grid numbers are 64^3 for A and C and 128^3 for B and D.

6.4.3. Box Refinement and Numerical Convergence

In the end, we mention about the influence of AMR refinement procedures during the collapse and about the numerical convergence. In GRMHD models, we refine the AMR blocks as the central density grows to save the computational time. Typically the total number of AMR blocks increases

from $\sim \mathcal{O}(10^2)$ at initial to $\sim \mathcal{O}(10^{3-4})$ at core bounce. We check whether this refinement procedure breaks such as the Hamiltonian constraint or the ADM mass conservation.

In Fig.16, we plot the central lapse α , the error of the Hamiltonian constraint $C_{\mathcal{H}}(\times 10)$ (see, Eq. (54)) and the ADM mass normalized by its initial value of magnetorotational collapse of a $100M_{\odot}$ star with zero metallicity (Umeda & Nomoto 2008). Such a highly massive star is considered to form BH and a good objection to test our GRMHD code. Initial conditions and the adopted EOS are the same as those used in model "GB12R020Sf" (see, Sec.7) and the minimum cell width is $\Delta x = 600\text{m}$. We also plot the deviation of the total angular momentum along the rotational axis from its initial value $|\Delta J_z| = |(J_z - J_{z,0})/J_{z,0}|$, here J_z is defined by Eq. (59) and $J_{z,0}$ is the value at $t = 0$ ms. In this test, the total number of AMR blocks increases from 792 to 11432 through three times refinement procedures until the time of core bounce. The ADM mass and the total angular momentum should be almost constant until the core bounce and for a short while after it. This is because it takes $5000\text{km}/c \sim 10\text{ms}$ till the gravitational radiation, emitted at core bounce around the center, reaches the outer boundary 5000km . From this test, we find that the total angular momentum are conserved within $\sim 1\%$ until the time of core bounce. In addition, the time evolution of the central lapse is smooth and no influence of the refinement procedures is seen. As for the Hamiltonian constraint, $C_{\mathcal{H}}$ is kept within several percentage until the time of core bounce except $t = 28 \sim 31$ ms and after a short while from the core bounce. We consider that the sudden increase of $C_{\mathcal{H}}$ during $t = 28 \sim 31$ ms is due to the low resolution and thus the next refinement at $t \sim 31$ ms suppresses the error. After the core bounce at $t \sim 32$ ms, $C_{\mathcal{H}}$ increases gradually due to the collapse but not rapidly and finally the calculation is crushed. We found the apparent horizon (Shibata 1997) is formed at the end of the calculation and we thus consider the BH is born.

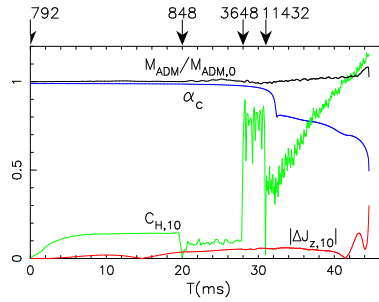


Fig. 16.— The Hamiltonian constraint $C_{\mathcal{H}}(\times 10)$ (*green*), the central lapse α (*blue*), the deviation of the total angular momentum $|\Delta J_z|(\times 10)$ (*red*) and the ADM mass normalized by its initial value (*black*) are plotted against time. Refinement procedures and enforcing the Hamiltonian constraint are done four times at when arrows point in the top. Initial ADM mass is $4.337M_{\odot}$ and the total number of AMR blocks is increased as 792, 848, 3648, and 11432.

In Fig. 17, we display magnified views of Fig. 16 around the time of core bounce with two different numerical resolutions. We put the outer boundary at 5000 km for lower resolution model and 4000 km for higher one and maintain the AMR structure almost the same in both models.

Then the cell widths of the higher resolution model are 0.8 times smaller than those of lower resolution model. In Fig. 17, *dashed* and *solid* lines correspond to higher (minimum cell width is $\Delta x = 480\text{m}$) and lower ($\Delta x = 600\text{m}$) resolution model, respectively. From this figure, we see that the good numerical convergence is achieved.

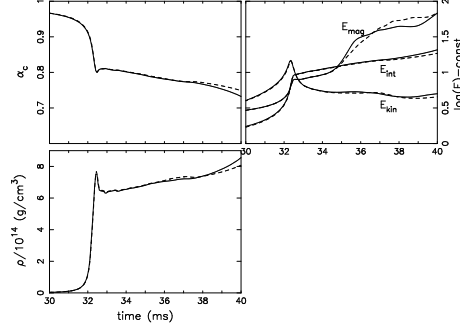


Fig. 17.— Time evolutions of the central lapse (*top-left*), various total energies (*top-right*) and the maximum density (*bottom-left*) with different numerical resolutions. The minimum cell widths are set as $\Delta x = 600\text{m}$ for *solid* lines and as $\Delta x = 480\text{m}$ for *dashed* lines. The internal, kinetic and magnetic energies are normalized by 10^{52} , 10^{51} and 10^{48} , respectively.

7. Collapse of a $15M_{\odot}$ Star

In this section, we calculate magneto rotational collapse of a $15M_{\odot}$ progenitor star as our practical test using GR/NMHD codes and check their abilities. We follow the gravitational collapse with varying the initial magnetic field, the stiffness of the EOS and the initial central angular velocity. We first describe our initial setups and then show results after subsection 7.4.

7.1. Equation of State

We adopt a parametric type EOS (e.g., Takahara & Sato 1988) in this study. It is divided into two parts, "cold" and "thermal" part. The cold part is expressed as

$$P_c = \begin{cases} K_1 \rho^{\Gamma_1} & 0 \leq \rho < \rho_1 \\ K_2 \rho^{\Gamma_2} & \rho_1 \leq \rho < \rho_2 \\ K_3 \rho^{\Gamma_3} & \rho_2 \leq \rho < \rho_3 \\ K_4 \rho^{\Gamma_4} & \rho_3 \leq \rho < \rho_4 \end{cases} \quad (76)$$

where, we fix $K_1 = 2.78 \times 10^{14}$ in cgs units and $K_{2,3,4}$ are determined from the continuity of P_c at $\rho_{1,2,3}$. ρ_3 corresponds to the nuclear density ρ_{nuc} . Polytropic indexes represent physical processes occurring during core collapse such as the electron-capture, onset of the neutrino-trap and the

nuclear repulsive force. We adopt two types of polytropic indexes and, for convenience, we call "Soft" and "Stiff" EOS as summarized in Table 1. Stiff EOS corresponds to the models reported in Mikami et al. (2008) and Soft EOS adopts smaller polytropic index compared to the Stiff case in the range of $\rho_1 \leq \rho < \rho_2$. That density region corresponds to the electron capture regime.

The thermal part is expressed by

$$P_t = (\Gamma_t - 1)\rho\varepsilon_t \quad (77)$$

and we fix the index of the thermal part as $\Gamma_t = 1.3$ in this study. Then the total pressure p and internal energy ε contributed from both thermal and cold part are written by

$$p = P_c + P_t \quad (78)$$

$$\begin{aligned} \varepsilon &= \varepsilon_t + \varepsilon_c \\ &= \varepsilon_t + \int_0^\rho \frac{P_c(\rho')}{\rho'^2} d\rho' \end{aligned} \quad (79)$$

7.2. Grid Setup

In NMHD models, we did not change their initial AMR structures and fixed them. On the other hand, we turn on the switch of AMR and refine AMR boxes in the vicinity of center in GRMHD models. This is because, the time step ΔT to keep the Courant-Friedrichs-Lewy condition (CFL condition) is determined from the maximum wave speed which usually becomes that of dynamical background and not hydrodynamical wave speed (i.e., the fast magneto sonic) in GRMHD models. The wave speed of the dynamical background is nearly the speed of light c and hardly change throughout the time evolution and also not depend on the hydrodynamical properties such as maximum density. We set ΔT as $0.3\Delta x_{\min}/c$ in GRMHD models to keep the CFL condition where Δx_{\min} is the minimum cell width in the computational domain. If we set maximum L_{AMR} as the maximum allowed one ($L_{\text{AMR},\max} = 8$ or 9 in this study) from the beginning of calculation,

Table 1. Parameters of cold part EOS

i	Soft EOS			Stiff EOS		
	$\rho_i (\text{g cm}^{-3})$	K_i	Γ_i	$\rho_i (\text{g cm}^{-3})$	K_i	Γ_i
1	4×10^9	2.78×10^{14}	4/3	4×10^9	2.78×10^{14}	4/3
2	1×10^{12}	7.25×10^{14}	1.29	1×10^{12}	4.66×10^{14}	1.31
3	2×10^{14}	3.17×10^{14}	1.32	2.8×10^{14}	2.45×10^{14}	4/3
4	1×10^{16}	4.22×10^{-3}	2.5	1×10^{16}	3.42×10^{-3}	2.5

it takes too much time until corebounce since the time step depends solely on Δx_{\min} . Therefore in GRMHD models, we set maximum L_{AMR} as 5 at the beginning and then increment it as the collapse proceeds to save computational time. We define the criterion to increment the maximum AMR level (i.e., refine the AMR boxes in the vicinity of center) that every time the central density exceeds 10^{11} , 10^{12} , $10^{13} \text{ g cm}^{-3}$. Influences of box refinements are described in Sec. 6.4.3.

The outer boundary is taken at 5000 km from the origin and $8 \times 8 \times 8$ AMR boxes with 0 refinement level ($L_{\text{AMR}} = 0$) cover the whole computational domain which is $(x, y, z) = [-5000, 5000] \text{ km}$. We set the maximum allowed AMR refinement level to 8 in standard model and to 9 for high resolution model, thus the highest resolution is $\Delta x \sim 600 \text{ m}$ in standard and $\Delta x \sim 300 \text{ m}$ in high resolution run. In standard models, the central region of $(x, y, z) = [-60, 60] \text{ km}$ is covered by $L_{\text{AMR}} = 7$ and $|x, y, z| \lesssim 30 \text{ km}$ is covered by $L_{\text{AMR}} = 8$ (see, Fig.18). On the other hand in high resolution run, the central regions of $|x, y, z| \lesssim 120, 60, 30 \text{ km}$ are covered by $L_{\text{AMR}} = 7, 8, 9$, respectively. Since the most dynamical and active region is above the surface of central core ($r \gtrsim 20 \text{ km}$) and inside the prompt shock ($r \lesssim 200 \text{ km}$), we increase resolutions as much as possible in this region. Then the total numbers of AMR blocks become ~ 6000 in standard run and ~ 42000 in high resolution run.

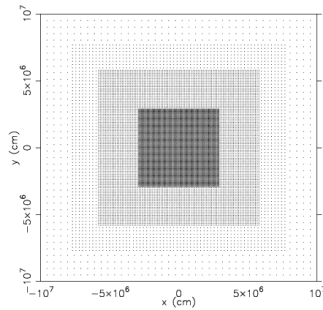


Fig. 18.— Schematic figure of grid setup in standard resolution run. Each point represents center of cell. The central region of $|x, y, z| \lesssim 30$ and 60 km is covered by $L_{\text{AMR}} = 8$ and 7 , respectively. In high resolution run, the central region of $|x, y, z| \lesssim 30, 60$ and 120 km is covered by $L_{\text{AMR}} = 9, 8$ and 7 , respectively.

7.3. Initial Setup

Our progenitor is a $15M_{\odot}$ star with the metallicity $Z=0.02$ and the pre-collapse model is taken from Umeda & Nomoto (2008) which calculates stellar evolution with spherical symmetry. We add rotation and magnetic field to the spherical progenitor model. Since little is known about the rotational law and magnetic field configuration in the central iron core and its surroundings at the

pre-collapse stage, we assume the rotational law such as

$$\Omega(\varpi) = \Omega_0 \frac{\varpi_0^2}{\varpi_0^2 + \varpi^2} \quad (\text{for NMHD}) \quad (80)$$

$$u^t u_\phi = \varpi_0^2 (\Omega_0 - \Omega) \quad (\text{for GRMHD}) \quad (81)$$

Where $\varpi = \sqrt{x^2 + y^2}$, $u_\phi = \sqrt{u_x^2 + u_y^2}$ and ϖ_0 is the parameter which is set as 10^8cm in this study. These configurations are commonly used rotational law in which the core, within $\sim \varpi_0$, rotates rigidly with angular velocity Ω_0 and differentially beyond that. Both equations represent same rotational profile, since in the Newtonian limit of Eq. (81) becomes Eq. (80) by replacing $u^t \rightarrow 1$ and $u_\phi \rightarrow \gamma_{\phi\phi} v^\phi = \varpi^2 \Omega$, where $\gamma_{\phi\phi}$ is a component of cylindrical flat metric.

As for the initial magnetic field configuration, to ensure divergence-free constraint, we adopt the following form of vector potential (see, e.g., Takiwaki et al. 2009).

$$(A_r, A_\theta, A_\phi) = \left(0, 0, \frac{B_0}{2} \frac{R_0^3}{r^3 + R_0^3} \varpi \right) \quad (82)$$

Where B_0 & R_0 are the parameters and $r = \sqrt{x^2 + y^2 + z^2}$. R_0 is fixed as 10^8cm in this study. This vector potential represents almost uniform magnetic field within $\sim R_0$ and dipole-like magnetic field configuration beyond $\sim R_0$ with the central magnetic field strength $\sim B_0$. We calculated several models with various initial magnetic field strength B_0 , in Eq. (82), and central angular velocity Ω_0 , in Eq. (80-81). We also add random perturbation to trigger asymmetric motion in the form of velocity with 5% amplitude when the maximum density exceeds 10^{13}g cm^{-3} . Such perturbation is added in the central sphere of radius 10^8cm via

$$\mathbf{u} = \mathbf{u} \left(1 + \sigma \frac{1}{1 + (r/R_0)^2} \right) \quad (83)$$

In this equation, R_0 is a parameter fixed with $R_0 = 10^8 \text{cm}$ and $-0.05 \leq \sigma \leq 0.05$ is a random number. Here, we have to comment about the momentum constraint, Eq.(53), in GRMHD model, since the momentum constraint would be violated by adding the perturbation. In our practical simulations, the momentum constraint \mathcal{M}_i is not kept strictly 0 during time evolution due to the numerical error. In our GRMHD model "GB12R020Sf", for instance, $C_{\mathcal{M}_x}$ defined by Eq.(84) is $C_{\mathcal{M}_x} \sim 1.53 \times 10^{-2}$ before the perturbation is added.

$$C_{\mathcal{M}_i} = \frac{1}{M_{\text{bar}}} \int \rho_* \mathcal{M}_i dx^3 \quad (84)$$

By adding the perturbation, this value increases to $C_{\mathcal{M}_x} \sim 1.55 \times 10^{-2}$. On the other hand, the error after core bounce is around $C_{\mathcal{M}_x} \sim 4.5 \times 10^{-2}$ in both models with and without the perturbation and we thus consider that the violation of the momentum constraint by the perturbation is negligibly small within the range of our numerical accuracy.

Model names and adopted parameters are summarized in Table 2. The first character "N" and "G" of model names indicate that the calculation is done by NMHD and GRMHD code,

respectively. Numbers after "B" and "R" represent the exponent of magnetic field strength and the central angular velocity, respectively. The last characters St/Sf represents Stiff/Soft EOS adopted. As for the initial magnetic field strength, we adopted 0, 10^9 and 4.8×10^{12} G so that we can easily check the roles of magnetic field.

The initial magnetic field is first amplified mainly through the compression and the rotational winding effects during collapse from previous many studies (e.g., Shibata et al. 2006; Burrows et al. 2007; Takiwaki et al. 2009). For instance, the compression mechanism amplifies the magnetic field about $\sim 10^3$ times (Burrows et al. 2007) and then $B_0 \sim \mathcal{O}(10^{12})$ G is amplified to $\sim \mathcal{O}(10^{15-16})$ G which is equivalent strength to that of magnetar (Duncan & Thompson 1992). Heger et al. (2005) studied stellar evolution with including magnetic field and rotation and they reported the strength of magnetic field is of the order of $\sim 10(9)$ G or weaker and the poloidal magnetic field is much weaker, approximately 10^{-4} , than the toroidal component. Thus our initial condition with purely poloidal and extremely strong magnetic field might be unrealistic one, however we employ such initial condition to see the effects of magnetic field easily and also to compare our results with other previous studies. In addition to the very strong initial magnetic field models, we calculated one model (NB09R02Sf) with initially weak magnetic field $B_0 = 10^9$ G in a high resolution run. Since, there are possibly several non linear magnetic field amplification mechanisms in the vicinity of PNS such as MRI or dynamo mechanism which are intrinsically 3D phenomena, we examine how the initially weak magnetic field is amplified through this model.

As for the central angular velocity Ω_0 we adopt 2 or 6 (rad/s). In Hirschi et al. (2004), they calculated the evolutions of various rotating stars with changing initial stellar mass and metallicity. Their results are that $25M_\odot$ star with solar metallicity ($Z = 0.02$) has $\Omega_0 \sim 1.0 \text{ s}^{-1}$ at the end of silicon burning stage. They also reported that lower initial metallicity raises the final angular velocity due to lower mass loss rate. Yoon & Langer (2005) did similar works to Hirschi et al. (2004), though they included magnetic effects. Their results showed magnetic torques lower the local specific angular momentum approximately one order of magnitude compared to non-magnetic field cases. However these two works are done by one dimensional calculations and are not still conclusive results. Thus, even though our adopted parameters are comparatively faster than the theoretical works those values may be reasonable.

7.3.1. Initial Setup for GRMHD

In GRMHD calculations, we have additional setups to be done which are constraining the Hamiltonian and momentum equations (52) and (53). To solve Eqs. (52-53), we assume conformally flat metric for initial condition, in which $\tilde{\gamma}_{ij} = \delta_{ij}$ (therefore, $F_i = 0$) and $K = 0$. Then, following (Shibata & Uryū 2002), constraint equations become the following 4 equations to obtain rest of BSSN variables ϕ and \tilde{A}_{ij} and gauge variables α and β_i .

$$\Delta_{\text{flat}} e^\phi = -2\pi S_0 e^{-\phi} - \frac{1}{8} \delta^{ik} \delta^{jl} \tilde{A}_{ij} \tilde{A}_{kl} e^{5\phi} \quad (85)$$

$$\Delta_{\text{flat}}(\alpha e^\phi) = 2\pi\alpha e^{5\phi}(S_0 e^{-6\phi} + 2\gamma^{ij}S_{ij}) + \frac{7\alpha e^{5\phi}}{8}\delta^{ik}\delta^{jl}\tilde{A}_{ij}\tilde{A}_{kl} \quad (86)$$

$$\delta_{ij}\Delta_{\text{flat}}\beta^j + \frac{1}{3}\beta^k{}_{,ki} - 2\tilde{A}_{ik}\delta^{kj}\left(\alpha_{,j} - \frac{6\alpha}{e^\phi}e^\phi{}_{,j}\right) = 16\pi\alpha S_i e^{-6\phi} \quad (87)$$

$$\tilde{A}_{ij} = \frac{1}{2\alpha}\left(\delta_{ik}\beta^k{}_{,j} + \delta_{jk}\beta^k{}_{,i} - \frac{2}{3}\delta_{ij}\beta^k{}_{,k}\right) \quad (88)$$

Where Δ_{flat} is the Laplacian in flat space. We solve above 4 equations by iterative method with initial guess as $\phi = 0$, $\tilde{A}_{ij} = 0$, $\alpha = 1$, $\beta^i = 0$. Then first, we evaluate conservative variables \mathbf{Q} from given metrics and primitive variables \mathbf{P} from a progenitor model. Second, we solve above each equation. We iterate these two procedures until sufficient convergence is achieved. After these procedures, the Hamiltonian constraint $C_{\mathcal{H}}$ at initial is kept below arbitrary chosen small number (in our calculations 10^{-8} is adopted).

7.4. Results

7.4.1. Global Dynamics

We first show the time evolutions of the maximum density ρ_{max} in Fig.19, which tells us rough overview of how the core collapse proceeds. In this study our calculations are done in full three-dimension and the central density does not always become the maximum one, thus we do not use central value. However all of our models show that the maximum density exists nearly the center. In Fig.19, each line corresponds to different model and the model names are shown in the bottom part. From this figure, we can find ρ_{max} is increased $\sim 30\%$ in GRMHD models when compared with corresponding NMHD models (e.g., "GB12R020Sf" vs "NB12R020Sf"). We however do not see any rapid increase of ρ_{max} which possibly indicates collapse toward BH formation. Another feature is that the central density gradually increases after core bounce when the magnetic field exists, on the other hand the central density decreases in non-magnetized models (e.g., *black* vs *red* solid curves). This difference means that the magnetic torque works strongly and the maximum density

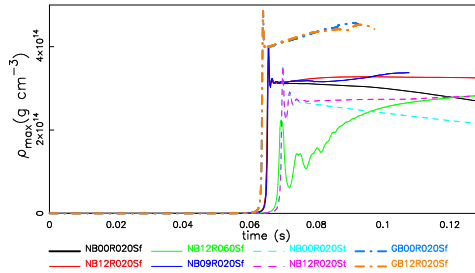


Fig. 19.— Time evolutions of the maximum density in different models. Model names are listed in the bottom.

increases due to the angular momentum transfer. In rapidly rotating model "NB12R060Sf", the

maximum density at core bounce marginally exceeds the nuclear density ($\rho_{\text{nuc}} = 2 \times 10^{14} \text{ g cm}^{-3}$) and it is thus not rotational supported core bounce but due to the nuclear repulsive force which is the same as the rest of models. In this model, ρ_{max} eventually relaxes to similar value to other models after several oscillations. We also summarize physical properties at core bounce in Table 3.

Fig. 20 displays time evolution of density profiles along the x axis in model NB12R020Sf(*left*) and NB12R020St(*right*). Numbers beside each line denote time in ms. Prompt shock which is

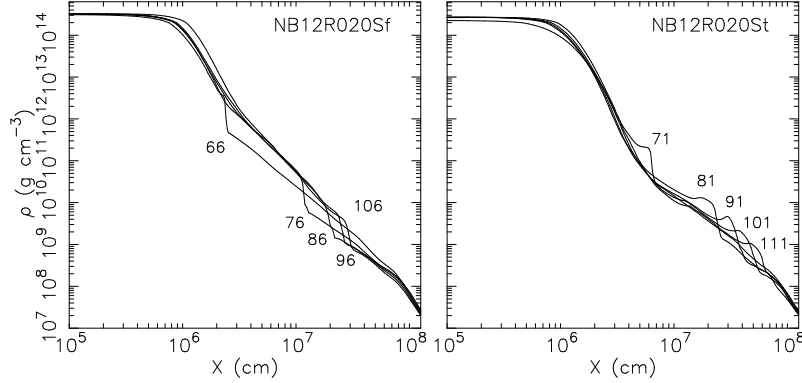


Fig. 20.— Density profiles along the x axis in model NB12R020Sf(*left*) and NB12R020St(*right*). Numbers denote time in ms.

formed at core bounce moves outward and then stays around $x \sim 200\text{-}300\text{ km}$ in model NB12R020Sf, on the other hand the shock moves further out in stiff EOS model NB12R020St. Model NB12R020St adopts same EOS as that of Mikami et al. (2008) and our result seen in the prompt shock propagation agrees well with their results.

In Fig.21, we display time evolutions of the rotational, internal and magnetic energies in *left* four panels and we also plot comparison between GRMHD(GB12R020Sf) and NMHD(NB12R020Sf) models in *right* two panels. The magnetic energy of model "NB09R020Sf" is too small compared to other strong field models and we display it separately with different range in *bottom-right* panel. We see that the rotational and the internal energies are kept almost constant or gradual increase after core bounce, on the other hand the magnetic energy increases rapidly, approximately ~ 2 orders, after core bounce. In strongly magnetized models (*upper-middle* panel), the final magnetic energies saturate around $\sim 5 \times 10^{50} \text{ ergs}$. When we compare GRMHD and NMHD models, shown in *right* two panels, the evolution tracks look similar except E_{rot} and E_{mag} after $t \gtrsim 80 \text{ ms}$. We consider the difference is originated from the bipolar-outflow and will be described in Sec. 7.4.2.

Finally we compare our results shown here with those reported by other groups. Obergaulinger et al. (2006) reported magnetorotational collapse in axisymmetry with various initial rotation, magnetic field and EOS and also with including general relativistic effects by replacing spherical Newtonian potential with "Tolman-Oppenheimer-Volkoff" potential. They showed that maximum rest mass

Table 2. Initial parameters and adopted EOS

model name	$B_0(\text{G})$	$\Omega_0(\text{rad/s})$	β_{mag}	$\beta_{\text{rot}}(\%)$	$E_{\text{grv}}(\text{ergs})$	α_c	M_{bar}/M_\odot	M_{ADM}/M_\odot	EOS
NMHD									
NB00R02St	0E0	2	0E0	0.135	-6.46E51	...	2.0483	...	Stiff
NB12R02St	4.8E12	2	2.95E-4	0.135	-6.46E51	...	2.0483	...	Stiff
NB00R02Sf	0E0	2	0E0	0.135	-6.46E51	...	2.0483	...	Soft
NB12R02Sf	4.8E12	2	2.95E-4	0.135	-6.46E51	...	2.0483	...	Soft
NB12R06Sf	4.8E12	6	2.95E-4	1.22	-6.46E51	...	2.0483	...	Soft
NB09R02Sf ¹	1E9	2	1.15E-11	0.135	-6.46E51	...	2.0483	...	Soft
GRMHD									
GB00R02Sf	0E0	2	0E0	0.132	-6.62E51	0.994	2.0688	2.0673	Soft
GB12R02Sf	4.8E12	2	2.00E-4	0.132	-6.62E51	0.994	2.0688	2.0673	Soft

¹This model is calculated with high resolution.

Note. — Each column denotes model name and initial parameters. From left; model name; magnetic field B_0 ; central angular velocity Ω_0 ; $\beta_{\text{mag}} = E_{\text{mag}}/|E_{\text{grv}}|$; $\beta_{\text{rot}} = T_{\text{rot}}/|E_{\text{grv}}|$; gravitational energy E_{grv} ; central lapse; baryon rest mass M_{bar}/M_\odot ; ADM mass M_{ADM}/M_\odot ; and adopted EOS.

Table 3. Physical properties at core bounce

model name	$\rho_{\text{max}}/10^{14}(\text{g cm}^{-3})$	β_{mag}	$\beta_{\text{rot}}(\%)$	α_c
NMHD				
NB00R02St	3.54	0	3.62	-
NB12R02St	3.55	6.17E-4	3.58	-
NB00R02Sf	3.95	0	3.00	-
NB12R02Sf	3.96	5.88E-4	2.82	-
NB12R06Sf	2.25	165E-1	13.9	-
NB09R02Sf	3.98	2.88E-11	3.04	-
GRMHD				
GB00R02Sf	4.87	0	2.25	0.839
GB12R02Sf	4.87	2.31E-4	2.20	0.839

Note. — From left; maximum density ρ_{max} ; $\beta_{\text{mag}} = E_{\text{mag}}/|E_{\text{grv}}|$; $\beta_{\text{rot}} = T_{\text{rot}}/|E_{\text{grv}}|$; central lapse α_c at core bounce.

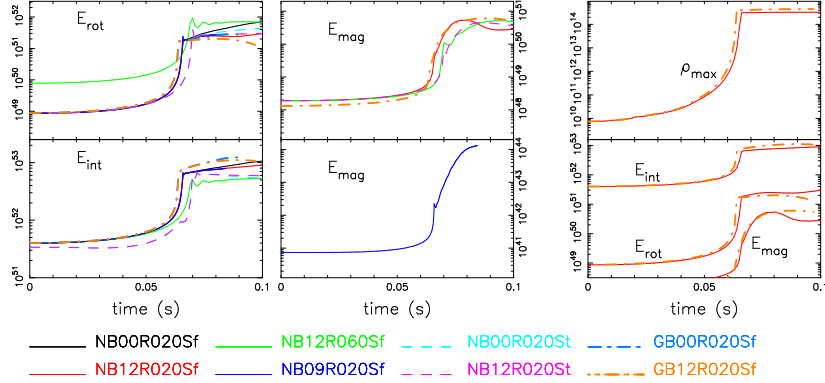


Fig. 21.— *Left* four panels; Evolutions of rotational, internal and magnetic energy. Initially weak magnetic field model "NB09R020Sf" is plotted with different range in the lower middle panel. *Right* two panels; Comparison between GRMHD(GB12R020Sf) and NMHD(NB12R020Sf) models. *Upper* and *lower* panels represent the maximum density and each energy component, respectively.

density is increased several 10 % after core bounce when they compare GR and Newtonian models and also that the magnetic field works to raise the maximum rest mass density. These features agree to ours since $\sim 30\%$ rise in the maximum density in our GRMHD model can be seen. Additionally, if we compare our results with previous three-dimensional NMHD work reported by Mikami et al. (2008), similar time evolutions are obtained such as time evolution of various energy components and also the shock propagation (as seen in Fig. 20). Thus, we consider the results shown here are common and robust features.

7.4.2. Formation of Outflow

Next, we describe the formation of bipolar outflow. In all of our strongly magnetized models, bipolar outflow is formed in a similar manner and we thus present mainly one representative model "NB12R020Sf" in this subsection. Fig.22 and Fig.23 show the density contour in model "NB12R020Sf" at different time slices. Fig.24 and Fig.25 are the same as Fig.22 but are with the color coded contour of plasma beta ($\beta_p \equiv P_{\text{gas}}/P_{\text{mag}}$) in logarithmic scale and the flow velocity in *white* arrows. *Black* curves represent the iso-density contour. The depicted region is $(x, y, z) = [-150, 150]\text{km}$ and, in each panel, *bottom-left*, *top-left* and *top-right* part represents *xy* (equatorial), *xz* and *yz* plane, respectively. As shown in these figures, the strongly magnetized regions where $\log \beta_p$ reaches ~ 0 appear along the rotational axis, which means the magnetic pressure is comparable to the matter pressure. Then high velocity outflow is launched along the rotational axis (see, Fig.26 for NMHD and Fig.27 for GRMHD) while inflow appears along the equatorial plane. On the other hand, non-magnetized models and weakly magnetized model "NB09R020Sf" do not form any bipolar outflow as seen from two *right* panels of Fig.26.

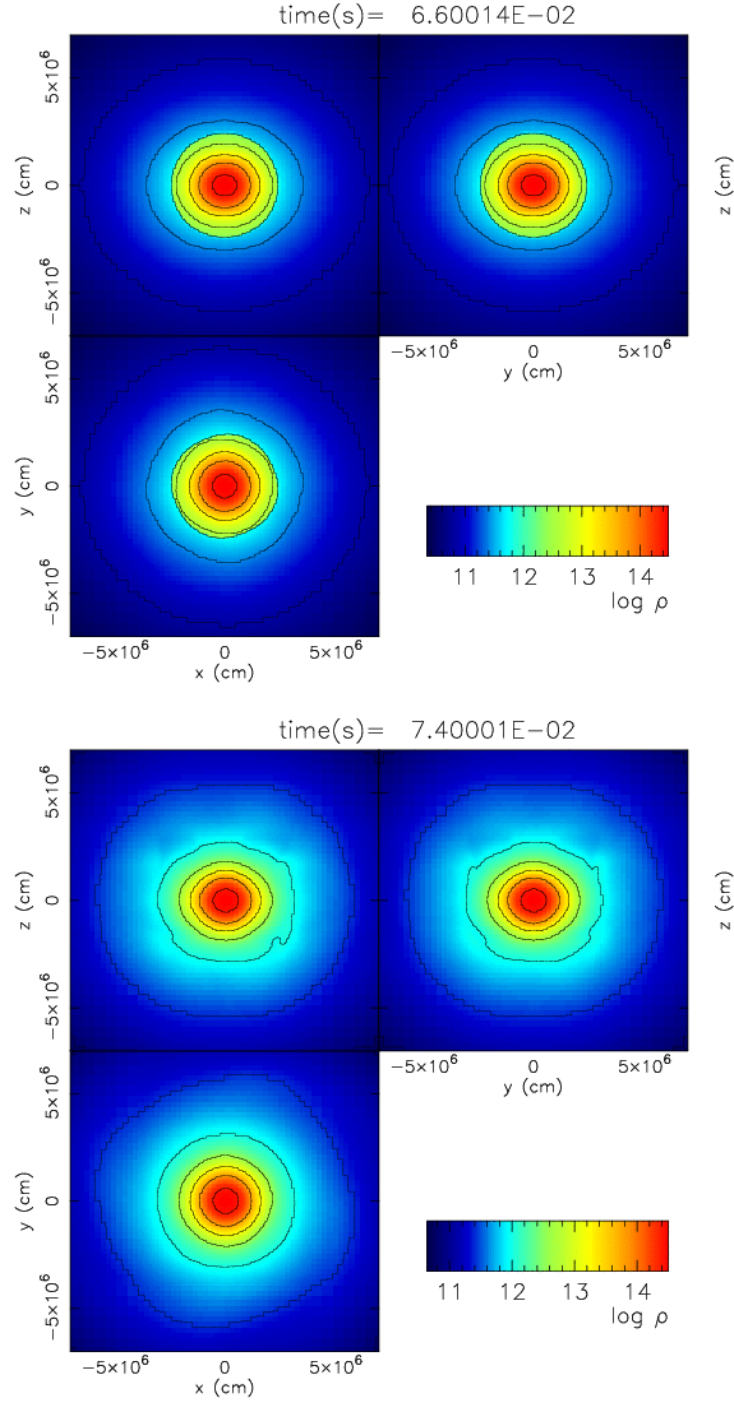


Fig. 22.— Logarithmic scale of rest mass density in model NB12R020Sf at different time slices are depicted. Time slices are chosen at $t=66\text{ms}$ (nearly the time of core bounce) and $t=74\text{ms}$.

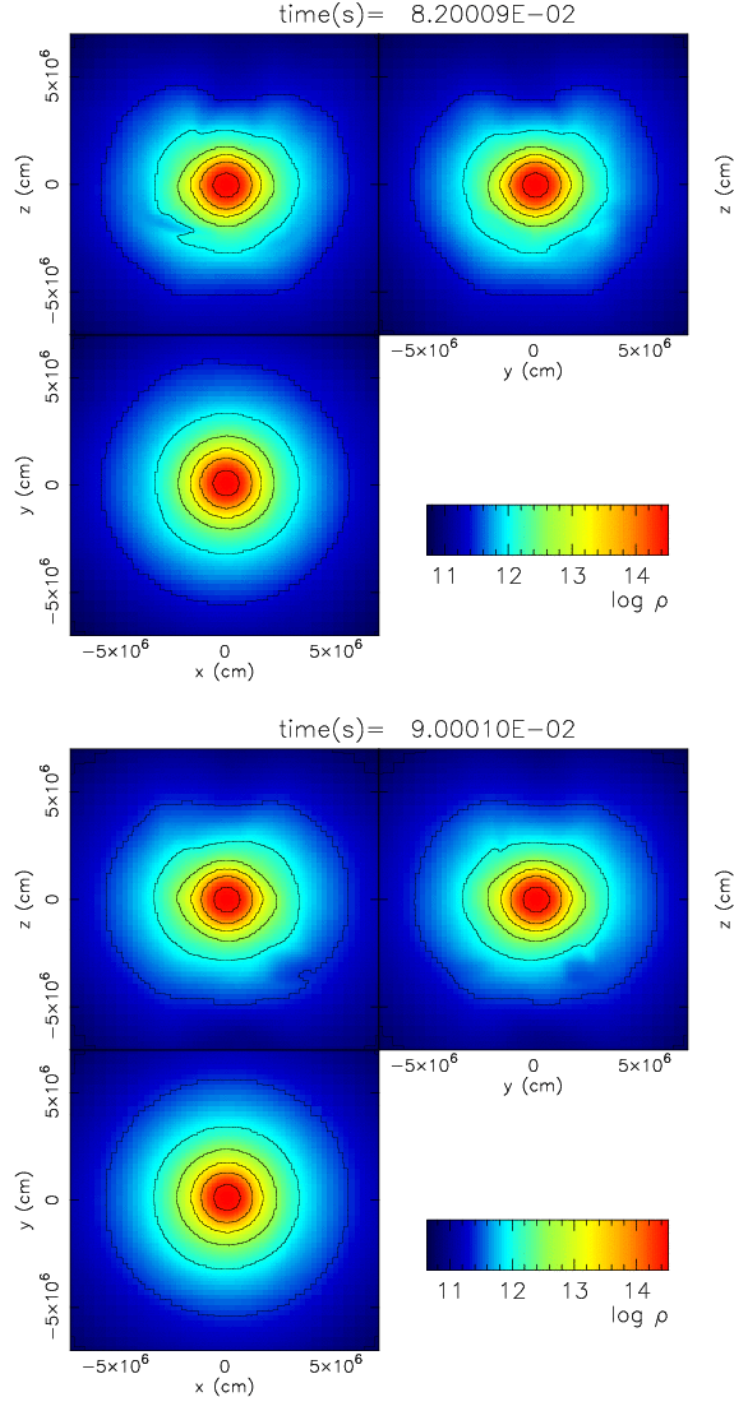


Fig. 23.— Same as Fig. 22 but for $t=82\text{ms}$ and $t=90\text{ms}$.

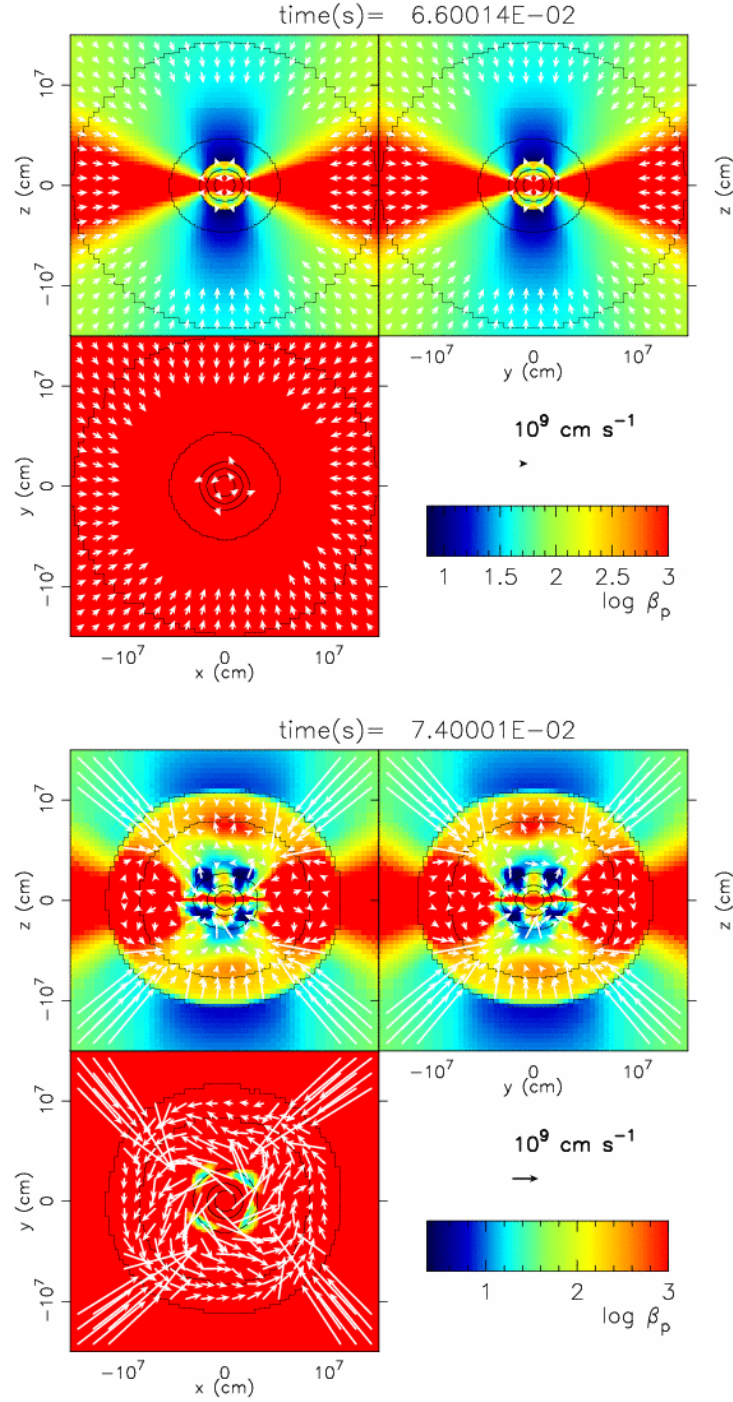


Fig. 24.— Logarithmic scale of plasma beta in model NB12R020Sf at different time slices are depicted. Time slices are chosen at $t=66\text{ms}$ (nearly the time of core bounce) and $t=74\text{ms}$. Arrows represent flow velocity and black curves represent iso-density contour. In the figure, we cut-off $\log \beta_p$ and the flow velocity higher than 3 and $3 \times 10^9 \text{ cm s}^{-1}$, respectively.

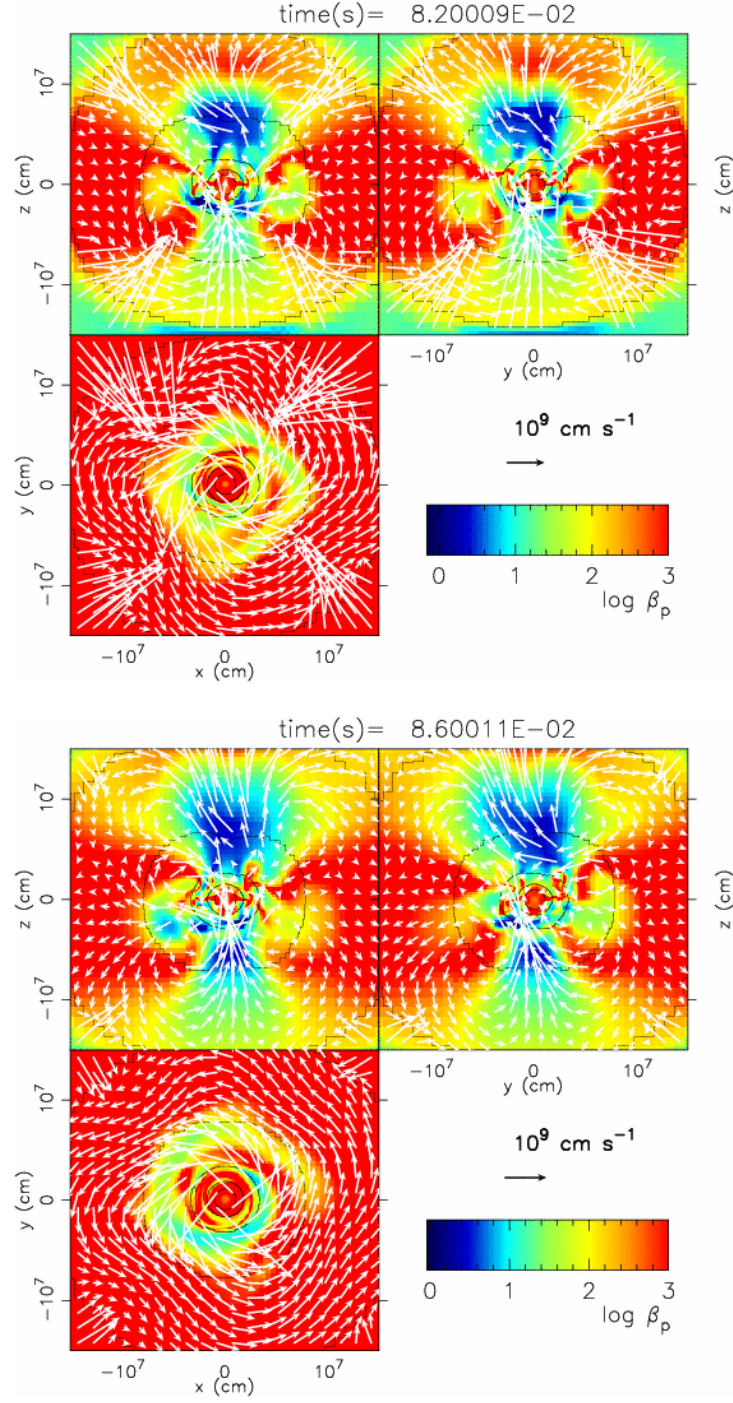


Fig. 25.— Same as Fig. 24 but for $t=82\text{ms}$ and $t=86\text{ms}$.

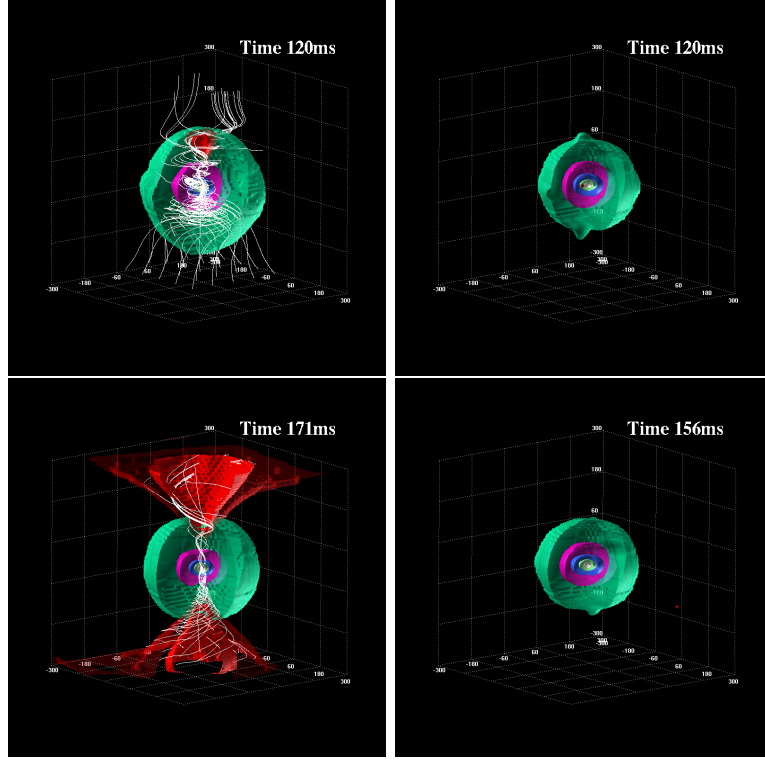


Fig. 26.— Three dimensional pictures of bipolar-outflow. *Left* two panels are "NB12R020Sf" and *right* two are "NB00R020Sf" and $|x, y, z| \leq 300\text{km}$ is drawn. The central spherical-like shells represent iso-density surfaces and the outermost shell (*green*) corresponds to 10^9g cm^{-3} . *White* lines are the magnetic field lines. Translucent and opaque *red* surfaces are iso-radial-velocity surfaces and each corresponds to $v_r = 10^9\text{cm s}^{-1}$ (translucent) and $v_r = 2 \times 10^9\text{cm s}^{-1}$ (opaque). In non-magnetized model "NB00R020Sf", high velocity bipolar outflow did not appear.

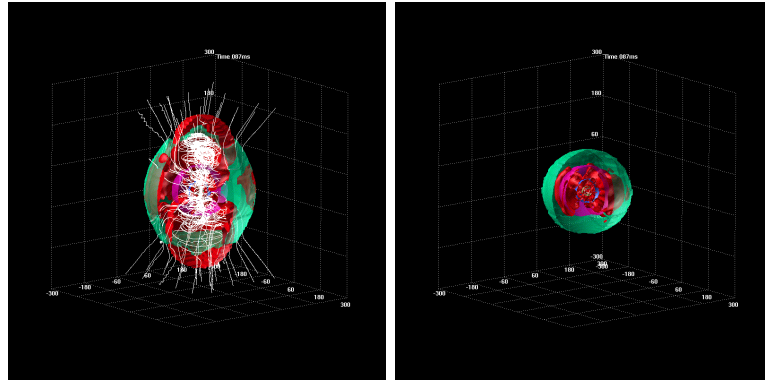


Fig. 27.— Same as Fig.26 but of GRMHD models (*left*; "GB12R020Sf" and *right*; "GB00R020Sf"). Both snapshots are taken at $t=87\text{ ms}$.

When we compare GRMHD(GB12R020Sf) and NMHD(NB12R020Sf) models, we see that the shock front of bipolar outflow moves faster, approximately a factor of 2, in GRMHD model as can be seen in Fig. 28. Since the bipolar outflow is driven by the angular momentum transfer (described in the next section), higher velocity outflow reflects that GB12R020Sf extracts larger angular momentum compared to NB12R020Sf. Then the magnetic energy is increased while the rotational energy is decreased as seen in *right-bottom* panel of Fig. 21.

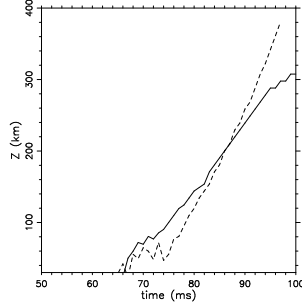


Fig. 28.— Time evolutions of the bipolar shock front along the rotational axis (Only those of north hemisphere are shown). *Solid* and *dashed* lines are results of NB12R020Sf and GB12R020Sf, respectively.

7.4.3. Driving Mechanisms of Outflow

In this section, we describe the driving mechanisms of the outflow. As mentioned in previous subsection, all strongly magnetized models exhibit high velocity outflow along the rotational axis. The ultimate energy source of outflow is the angular momentum transfer from the central object which can be seen from Fig.29. In this figure, the angular velocities along the x axis of different models at different time slices are shown. For instance, from left two panels, we can see the angular velocity within $x \lesssim 10\text{km}$ decreases rapidly, a factor of several, from $t = 66\text{ms}$ to $t \sim 80\text{-}90\text{ms}$. On the other hand, non-magnetized models (right two panels) do not show any deceleration (note that kink in the angular velocity profile at $x \sim 3\text{km}$ shown in $t = 120\text{ms}$ of "NB00R020Sf" is originated from such as meridional circulation or displacement of the mass center). From this fact, the angular momentum is extracted from the central object by the magnetic field. The extracted angular momentum is first converted to the magnetic field mainly via the magnetic field lapping. Then, there are two types of driving mechanisms of the outflow, the magneto-spring and the magneto-centrifugally supported mechanisms. We consider, from *left* two panels of Fig.26, that initial mechanism is the magneto-spring effect and then it transitions to the magneto-centrifugally supported mechanism. This is because from Fig.26, we see the magnetic field lines are highly twisted inside the shell at the onset of launching the outflow ($t=120\text{ms}$), however this twisted configuration is stretched eventually, as if the compressed spring would do, toward the north-south

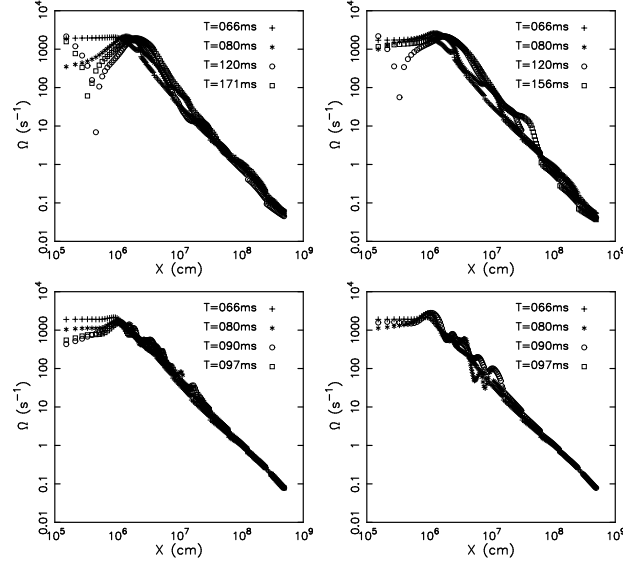


Fig. 29.— The angular velocity profiles along x axis at different time. From *top-left* to clock wise direction, "NB12R020Sf", "NB00R020Sf", "GB00R020Sf" and "GB12R020Sf" are displayed. Note that in all four models shown in this figure, the time of core bounce is approximately 66ms. Kinks, e.g., shown around $x \sim 3\text{km}$ in the *top-left* panel at $T = 120\text{ms}$, represent the retrograde of the angular velocity.

direction as seen in $t=171\text{ms}$ panel. Final magnetic field configuration is less toroidal dominant compared to that of $t=120\text{ms}$ and the matters stream away along these helical magnetic field lines. This is also seen in Fig.30 which shows time evolutions of the outflow velocity (V_z), the toroidal magnetic field (B_ϕ) and angle $\theta \equiv \cos^{-1}((\mathbf{B} \cdot \mathbf{V})/BV)$ between the magnetic field and the velocity vector, along the rotational axis of model "NB12R020Sf". From *upper-right* panel, we find the strongly amplified B_ϕ at $t \sim 120\text{ms}$ and $z \lesssim 80\text{km}$ which shortly disappears. At the same time, the high velocity region appears in the *upper-left* panel. The angle θ is nearly $\sim 90^\circ$ at $z \lesssim 50\text{km}$ and $t \gtrsim 120\text{ms}$ which indicates that the outflow is driven by the gradient of magnetic pressure (i.e., the magneto spring effect). Then V_z is accelerated up to $z \sim 110\text{km}$ along the magnetic field ($\theta \sim 0^\circ$, i.e., the magneto centrifugal effect).

In Shibata et al. (2006), they calculated 2D axisymmetric GRMHD simulations and reported MHD outflow is first driven by the magneto-spring effect and eventually by the magneto-centrifugally supported mechanism. Thus our results of launching processes of MHD outflow are qualitatively similar to theirs.

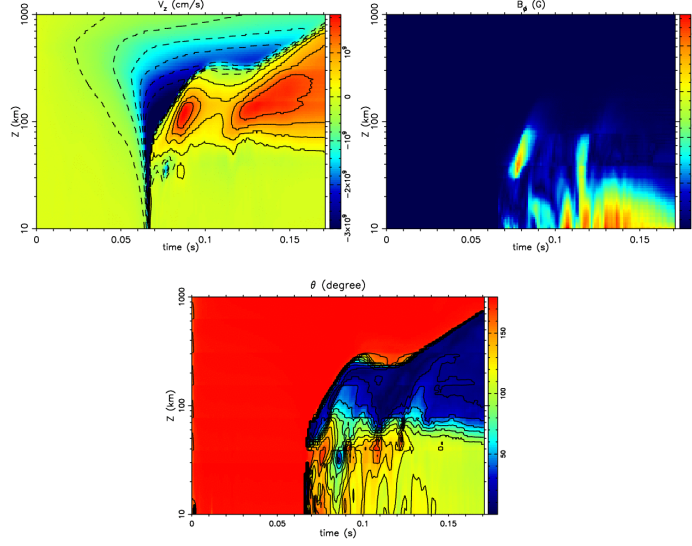


Fig. 30.— Time evolutions of the velocity component (V_z , *upper-left*), the toroidal magnetic field (B_ϕ , *upper-right*) and angle θ (*bottom*) between the magnetic field and the velocity vector, along the rotational axis of model "NB12R020Sf".

7.5. Non-Axisymmetric Motion

As described in the previous subsection, our results seen in dynamical evolutions are qualitatively the same as those reported in previous 2D axisymmetric MHD works (for NMHD see, e.g., Kotake et al. (2005); Sawai et al. (2005); Burrows et al. (2007) and for GRMHD see, e.g., Obergaulinger et al. (2006); Shibata et al. (2006)) in the way that the equatorial inflow and the bipolar outflow along the rotational axis due to the magnetic field. We also calculated several models with tilted magnetic field axis against the rotational axis to induce larger non-axisymmetry and found the outflow is driven along the rotational axis similar to Mikami et al. (2008). According to many previous studies, both in GR and the Newtonian limit (e.g., Ott et al. 2007; Scheidegger et al. 2009), the nascent neutronstar is sensitive to the rotational instability predominated by the "m=1" non-axisymmetric mode within our initial rotational parameter range. To confirm our code can actually reproduce some nonaxisymmetric modes characteristic to rotational collapse of massive stars, we monitor the non-axisymmetry with the same approach as Scheidegger et al. (2009). We decompose the density into the Fourier components along the equatorial ring of radius 40km which is beyond the central rigidly rotating region and inside the prompt shock (see, Fig.20). Fourier amplitude of mode "m" is defined as the following equations.

$$\rho(\varpi, z, \phi) = \sum_{m=-\infty}^{\infty} A_m(\varpi, z) e^{im\phi} \quad (89)$$

$$A_m(\varpi, z) = \frac{1}{2\pi} \int_0^{2\pi} \rho(\varpi, z, \phi) e^{-im\phi} d\phi \quad (90)$$

In Fig.31, we plot the time evolutions of normalized mode amplitude $|A_m|/|A_0|$. From this figure, we

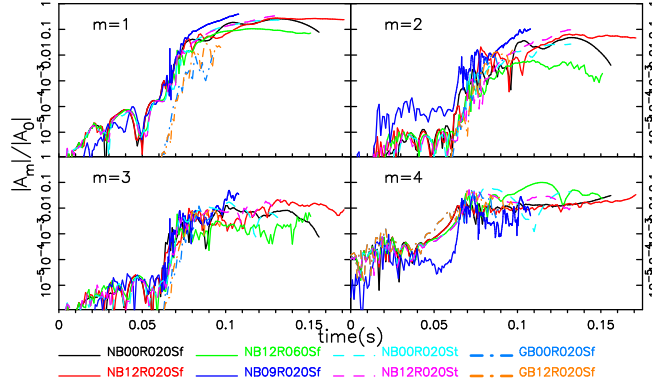


Fig. 31.— Time evolutions of the normalized mode amplitude $|A_m|/|A_0|$. Model names are listed in the bottom part.

see that $m=4$ mode is the most dominant mode before core bounce ($t \sim 66\text{ms}$) since our cartesian grid induces quadrupole numerical noise at initial. However, the linear amplification phase starts immediately after core bounce and several ms later it reaches the non-linear phase ($t \gtrsim 75\text{ms}$). During the non-linear phase, dominant mode becomes $m=1$ and their normalized amplitude exceed $\gtrsim 0.1$. This is consistent with the structure, a so-called one-armed spiral structure seen in Ott et al. (2005). Since β_{rot} at core bounce reaches $\sim 3\%$ and also keeps $\gtrsim 1\%$ after core bounce, we consider that the low- $|T/W|$ instability causes this non-axisymmetric configuration. Like these, even though the outflow structure is almost axisymmetric from broader perspective, non-axisymmetry develops and show significantly large mode amplitude in the vicinity of center in the self gravitating system. This non-axisymmetry may alter the gravitational wave form (Scheidegger et al. 2009).

Next, we describe about the amplification of initially weak magnetic field ($B_0 = 10^9\text{G}$) in model "NB09R020Sf". As mentioned above in Sec.7.4.2, only through the field-wrapping and the compression mechanism, the magnetic field cannot be amplified strongly enough to drive the outflow soon after the core bounce as seen in other models with initially strong magnetic field. However, there might be several magnetic field amplification mechanisms to be occurred after core bounce such as the MRI or the dynamo mechanism (Akiyama et al. 2003; Cerdá-Durán et al. 2007; Obergaulinger et al. 2009) in addition to the aforementioned linear mechanisms. If some of these mechanisms operate within dynamical time scale, the saturated magnetic field is considered to possess enough capability to affect the explosion dynamics. The largest difference between 3D and 2D(axisymmetric) in the amplification of the magnetic field is conversion from toroidal to poloidal magnetic field, since the toroidal to poloidal conversion can never happen in 2D axisymmetric motion. This is because, from the Faraday's law, time evolution of a poloidal component B^{pol} becomes

$$\partial_t B^{\text{pol}} + \partial_{\text{pol}\perp} (B^{\text{pol}} v^{\text{pol}\perp} - v^{\text{pol}} B^{\text{pol}\perp})$$

$$+ \partial_{\text{tor}}(B^{\text{pol}}v^{\text{tor}} - v^{\text{pol}}B^{\text{tor}}) = 0 \quad (91)$$

Here, "pol" and "tor" represent a poloidal and toroidal component, respectively, and "pol \perp " is a perpendicular one to both the "pol" and "tor" components. In axisymmetry, $\partial_{\text{tor}} = 0$ and thus B^{tor} cannot be converted to B^{pol} , however in full 3D, several non-axisymmetric fluid motions (e.g., the Parker or the Tayler or the convective instabilities) let $\partial_{\text{tor}} \neq 0$ and close the conversion cycle (i.e., from poloidal to toroidal and toroidal to poloidal). Through our weakly magnetized model "NB09R020Sf", we examine how the magnetic field is amplified after core bounce and whether the amplified magnetic field affect the explosion dynamics or not.

In Fig.32, we display time evolution of the magnetic field strength in logarithmic scale of model "NB09R020Sf" which is high resolution run. Within $r \lesssim 20\text{km}$, strength of the magnetic

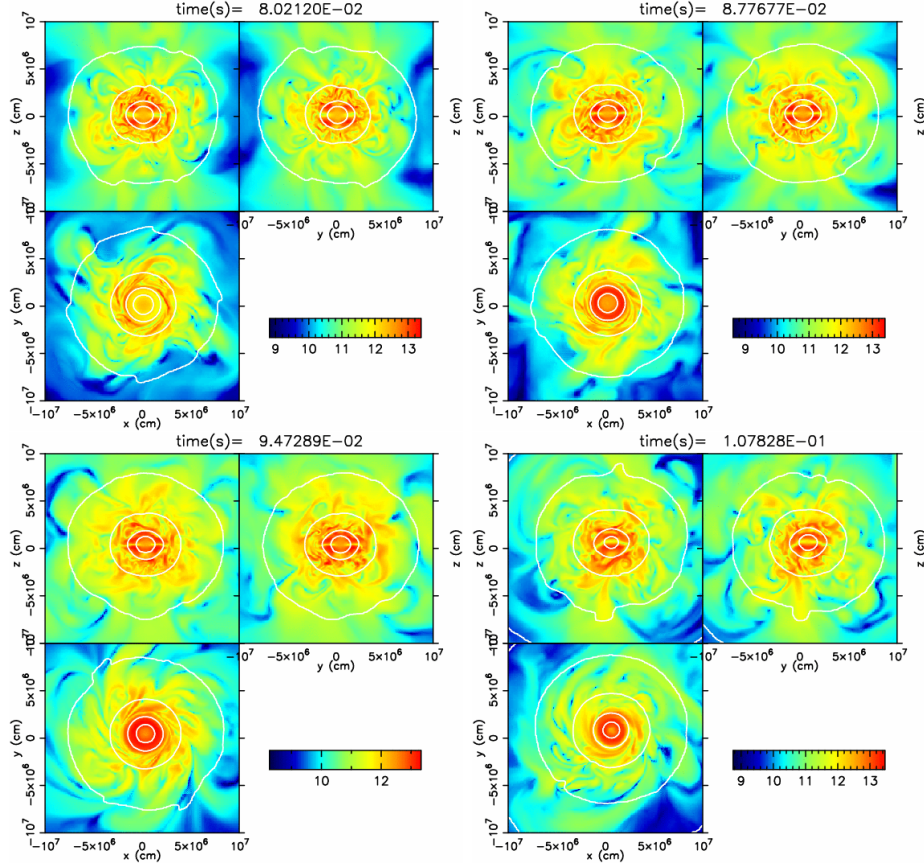


Fig. 32.— Time evolution of the magnetic field in logarithmic scale of model "NB09R020Sf".

field shows stratified configuration compared to $r \gtrsim 20\text{km}$ and is amplified strongest ($\sim 2 \times 10^{13}\text{G}$) among the numerical domain. Since, within $10 \lesssim r \lesssim 20\text{km}$, matters rotate differentially with the steepest angular velocity gradient (see, Fig.29), the magnetic field strength is higher than the value of central region $r \lesssim 10\text{km}$ where the rotation is almost rigid. Magnitude of the amplification is $\sim 10^{13}/10^9 = 10^4$ which is close to the value predicted by compression and we thus consider the

dominant field amplification mechanisms within $10 \lesssim r \lesssim 20\text{km}$ are compression and the rotational winding effect.

In contrast, we see the region $r \gtrsim 20\text{km}$ is highly non-homologous and the magnetic field configuration pattern changes momentarily, however the maximum strength keeps the same level of the order of $\lesssim 10^{13}\text{G}$ throughout our calculation ($\sim 40\text{ms}$ after core bounce). The stochastic configuration pattern beyond $r \sim 20\text{km}$ is mainly triggered by the entropy driven convection. The reason is like this. There are several candidates to configure such flow pattern such as the convective motion, the MRI, the Parker instability (or the magnetic buoyancy) or the Tayler instability. However, among them, the growth time scales of the Tayler and the Parker instabilities are too long and they are inefficient during our calculation time. For instance, the growth time scale of the Tayler instability is the order of the *Alfvén* crossing time of the system and $\sim \mathcal{O}(1)$ h according to Cerdá-Durán et al. (2007) in a weakly magnetized limit. As for the Parker instability, the growth time scale (τ_{mag}) can be estimated by using the frequency of the magnetic buoyancy N_{mag} as $\tau_{\text{mag}} \sim 2\pi N_{\text{mag}}^{-1}$. According to Acheson (1979), N_{mag} is defined by using the the *Alfvén* velocity c_A , the speed of sound a , the toroidal magnetic field B_ϕ and the rest mass density ρ as

$$N_{\text{mag}}^2 = \frac{c_A^2}{\gamma a^2} \mathbf{g} \cdot \nabla \left(\ln \frac{B_\phi}{\rho} \right) \quad (92)$$

Where, $\gamma \equiv d \ln p / d \ln \rho|_S$, S is the entropy and \mathbf{g} is the gravitational acceleration. In what follows, we adopt a pseudo-entropy defined by $S \equiv P_t / P_c$. In Fig. 33, we display color coded contour of N_{mag}^2 (*right*) in addition to the Brunt-Väisälä frequency N^2 (*left*) defined by

$$N^2 = \frac{1}{p\gamma} \frac{\partial p}{\partial S} \bigg|_\rho \mathbf{g} \cdot \nabla S \quad (93)$$

in log scale of model "NB09R020Sf". In each panel, color-less area is where N^2/N_{mag}^2 has positive value and is thus stable region against each mechanism. The specific angular momentum with positive gradient with respect to r has stabilizing effect on the convective motion, however it has negative gradient in our models and the unstable region becomes larger when we consider the contribution from it (i.e., the Solberg-Høiland criterion). From Fig. 33, we see the PNS is convectively and magnetic buoyantly unstable. However, the growth time scale of each mechanism differs widely, $\tau \sim 2\pi N^{-1} \sim 1 - 10\text{ms}$ for convection and $\tau_{\text{mag}} \sim 2\pi N_{\text{mag}}^{-1} \gtrsim 0.1 - 10\text{s}$ for magnetic buoyancy. Since our calculation time is $\sim 40\text{ms}$ after core bounce, the Parker instability does not grow while the convection can grow sufficiently within our simulation times. The convective-dynamo is thus considered to contribute to the magnetic field amplification mechanism.

We also examine the possibility of the MRI. Since, from local linear analysis, the MRI would occur when the rotation is differential with negative angular velocity gradient (Balbus & Hawley 1991). From Fig.29, we see inside the shock ($r \lesssim 100\text{km}$) has negative angular velocity gradient and is thus unstable against the MRI. However, to follow the MRI by numerical simulation, the critical wave length of the MRI " λ_{MRI} " has to be resolved at least ~ 10 numerical grids

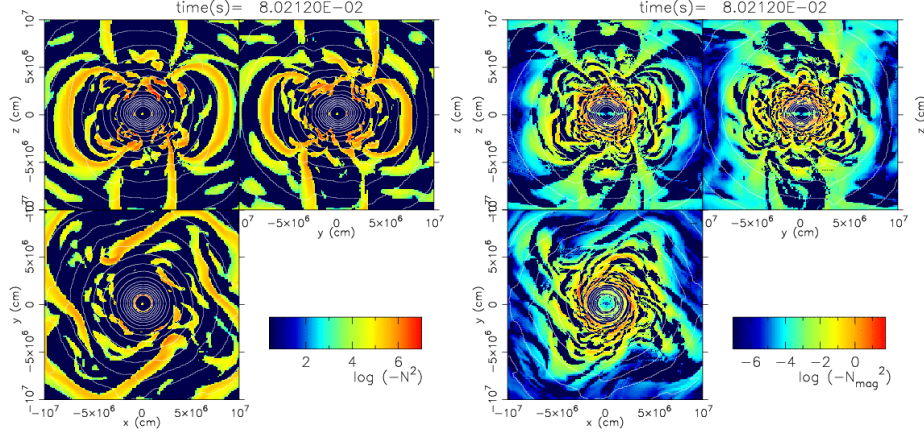


Fig. 33.— Logarithmic scale of the Brunt-Väisälä frequency $-N^2$ (*left*) and the magnetic buoyant frequency $-N_{\text{mag}}^2$ (*right*) of model "NB09R020Sf". Color-less area is where N^2/N_{mag}^2 has positive value (i.e., stable region) and *white* curves are the iso-density contour.

(Obergaulinger et al. 2009). Here, λ_{MRI} is defined by

$$\lambda_{\text{MRI}} = 4\pi c_A \left(-\varpi \frac{\partial \Omega^2}{\partial \varpi} \right)^{-1/2} \quad (94)$$

$$(95)$$

In Fig.34, we display the ratio of the critical wave length λ_{MRI} to the local numerical grid width in *left* panel and rough estimation of the growth time scale of the fastest growing MRI mode " $\tau_{\text{MRI}}(\text{ms})$ " in log scale in *right* panel. τ_{MRI} is defined by (see, Balbus & Hawley 1991).

$$\tau_{\text{MRI}} = 4\pi \left(\left| \varpi \frac{\partial \Omega}{\partial \varpi} \right| \right)^{-1} \quad (96)$$

From *left* panel of this figure, we see the most part has negative value and therefore the MRI cannot be resolved. We have to employ $\gtrsim 10$ times higher resolution ($\Delta x \lesssim 30 - 60\text{m}$) to resolve the MRI or, if we adopt ~ 10 times larger initial magnetic field ($\sim 10^{10}\text{G}$), we possibly manage to do it with our high resolution run marginally, since the wave length λ_{MRI} is proportional to $|B|$. Here, we comment about our strongly magnetized models ($B_0 \sim 10^{12}\text{G}$). If we extend what we mentioned just above (i.e., to adopt stronger initial magnetic field), we may easily resolve the MRI since the critical wave length λ_{MRI} is approximately 10^3 times larger compared to weakly magnetized model. From Fig. 34, we can estimate the wave length as $\lambda_{\text{MRI}} \sim 60\text{m}$ (*yellow* region) and $\lambda_{\text{MRI}} \sim 600\text{m}$ (*orange* region) for $30 \lesssim r \lesssim 60\text{km}$ where the resolution is $\Delta x \sim 600\text{m}$. Then in the strongly magnetized models, λ_{MRI} multiplied 10^3 becomes $\lambda_{\text{MRI}} \sim 60 - 600\text{km}$. However, the system scale (i.e., inside the prompt shock) is $\sim 200\text{km}$ and therefore those modes which have larger wave length than the system cannot last. In case an MRI mode lasts and if we can resolve

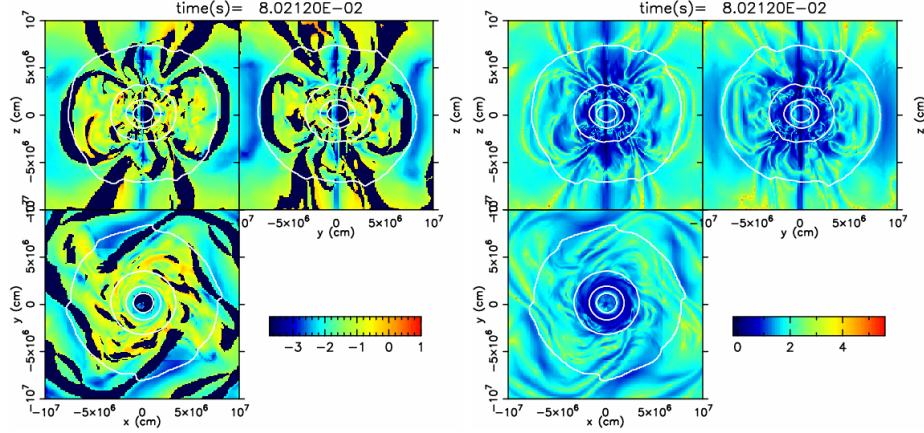


Fig. 34.— Contour of $\lambda_{\text{MRI}}/\Delta x$ (*left*) and τ_{MRI} (ms) (*right*) in log scale from model "NB09R020Sf". Colorless areas in *left* panel are where the MRI stable regions (i.e., positive angular velocity gradient).

it, the magnetic field soon reaches saturation strength in several times of the growth time scale. Akiyama et al. (2003) derived the saturated magnetic field strength $B_{\text{sat,MRI}}$ as

$$B_{\text{sat,MRI}}^2 \sim 4\pi\rho v_\phi^2 \quad (97)$$

and it becomes $\sim 10^{15}$ G with our initial rotational parameter. All of our strongly magnetized models exhibit saturated magnetic field strength of the order of $\sim 10^{15-16}$ G after core bounce (the value is consistent with those reported by previous many studies, e.g., for NMHD Kotake et al. (2005); Sawai et al. (2005); Burrows et al. (2007), for GRMHD, Obergaulinger et al. (2006); Shibata et al. (2006) and for 3D works, Mikami et al. (2008); Scheidegger et al. (2009)). The value is comparable to $B_{\text{sat,MRI}}$ and we thus consider the initially strong magnetic field is first amplified by the compression and the winding effect with the amplification magnitude of the order of $\sim 10^3$ and then the MRI operates to amplify the magnetic field up to the saturation strength (in Obergaulinger et al. 2006; Shibata et al. 2006, they reported the MRI operates with adopting similar initial magnetic field strength $\sim 10^{12}$ G). However, since just only the linear amplification mechanisms amplify the magnetic field up to $\sim 10^{15}$ G which is close to the MRI saturation level, to see the effects of the MRI amplification more clearly, we have to adopt sufficiently weak magnetic field (e.g., $B_0 \sim 10^{10}$ G) which does not reach $B_{\text{sat,MRI}}$ only through the linear amplification mechanisms but sufficiently strong to resolve by numerical simulation.

As for the calculation time, the length of 40 ms after core bounce is marginally sufficient for the inner region ($r \lesssim 40$ km) from the *right* panel of Fig. 34, however beyond that region we have to evolve more than several hundreds ms. If we capture the linear amplification, it may reaches the saturation phase within the several rotational periods. At this saturation phase, whether the magnetic field is sufficiently strong to affect the explosion dynamics and how the magnetic field configuration is cannot be clarified without numerical simulation and this would be our future work.

8. Summary and Discussions

The explosion mechanisms of the core-collapse supernovae have been unknown and fascinating problems for several decades. Recent observations show several common features seen in the CCSNe that some types of them are bipolar like and sometimes non-axisymmetric explosions. Motivated by these, we now have to take into account the effects of asymmetry into numerical works to uncover the explosion dynamics. Fortunately, recent development of computational resources enable us to handle the numerical simulations in the context of three dimension. We therefore have developed two types of three dimensional magneto hydrodynamical codes. One is in the Newtonian approximation (NMHD) and the other is in the full general relativity (GRMHD). The features of our codes are; (1) Adoptive Mesh Refinement to cover the wide dynamical ranges; (2) high resolution shock capturing scheme with Roe-like (in NMHD) and HLL (in GRMHD) flux; (3) several reconstruction schemes to maintain high spatial resolution; (4) time update of the matters and the metric is done by the iterative Crank-Nicholson scheme; (5) the constrained transport to evolve the magnetic field; (6) any types of the EOS can be adopted; (7) the Poisson solver with BiConjugate Gradient Stabilized Method under our AMR structure to solve the self gravity (in NMHD) and the non-linear Poisson like equations for the Hamiltonian and the momentum constrains (in GRMHD).

In this paper, we described our numerical methods in detail and did several tests to confirm their abilities through the simple shock tube tests; the Poisson solver for the spherically distributed matters; conservation of the mass, the energy and the local/global angular momentum; the quadrupole linearized gravitational wave; the rotating neutronstar in equilibrium states and so on. Through these tests, we confirmed that our codes reproduce the numerical error convergence predicted by our adopted reconstruction schemes and also confirmed that the accuracy of our code is sufficient to follow the dynamical evolution of CCSNe. And as for the first test of CCSN simulation, we calculated collapse of a $15M_{\odot}$ progenitor with varying the initial magnetic field strength, the angular velocity and the stiffness of the Polytropic EOS by our GRMHD and NMHD codes. Our main results and some discussions are as the following.

(1) After a short while ($\sim 20\text{ms}$) from the time of core bounce, high velocity ($V_r \sim 2 \times 10^9 \text{cm s}^{-1}$) bipolar outflow is driven from surface of the proto-neutronstar ($|z| \sim 30\text{km}$) and moves through along the rotational axis. The bipolar outflow does not appear in the non-magnetized and the initially weak magnetized models which indicate the outflow is magnetically driven outflow. The energy source of this outflow is the extracted angular momentum of the central proto-neutronstar which is transfered by the magnetic torque. The driving mechanisms are first by the magneto spring effect and then we consider the magneto centrifugally supported outflow.

(2) In our self gravitating system, the non-axisymmetry develops immediately after the core bounce with the linear amplification at first and soon reaches the non-linear phase. The dominant non-axisymmetric mode is the $m=1$ mode during the non-linear phase and the one-armed spiral structure is also can be seen. Since our initial rotational velocity ($\Omega_c \geq 2 \text{ rad/s}$) satisfies the low-

$|T/W|$ instability criterion ($\beta \gtrsim 1\%$) after core bounce, we consider that these non-axisymmetric, spiral mode is originated from the low- $|T/W|$ instability. However, these non-axisymmetric motions are confined in the vicinity of the center and, in general terms, the global structure of bipolar outflow is qualitatively the same as those reported in previous 2D axisymmetric MHD works in the way that the equatorial inflow and the bipolar outflow along the rotational axis.

(3) In weakly magnetized model in which the initial central, poloidal magnetic field is 10^9G , the convective over turn highly deforms the magnetic field configuration. However, with our resolution of $\Delta x \sim 300 - 600\text{m}$ and limited computational time ($\sim 40\text{ms}$ after core bounce), we did not find the exponential growth of the magnetic field which can be seen if the magneto-rotational instability works. If we employ 10 times higher resolution or 10 times stronger initial magnetic field, we possibly capture the MRI marginally. Time scale of the MRI is $\tau_{\text{MRI}} \sim \mathcal{O}(1)$ ms inside $r \lesssim 30\text{km}$ which is comparable to the dynamical time scale and is sufficiently short to follow by the numerical simulation. Even if the MRI operates in a weakly magnetized model, whether the MRI amplifies the magnetic field strongly enough to affect the explosion dynamics or not and whether the amplified magnetic field contributes to launch the outflow are big issues. Especially, since the the amplified magnetic field through the MRI would be less directional (i.e., the magnetic field is not amplified intensively along the rotational axis as seen in Fig.26 & 27), we have to examine whether the amplified magnetic field affect the magneto-rotational explosion scenario.

(4) By comparing GRMHD and NMHD models, we found that the gravitational effect works a little bit stronger in GRMHD models which can be seen in the increase of the central density as $\sim 30\%$. However, the global dynamical evolutions are similar such as the time of core bounce and formation of the bipolar outflow. Therefore we consider that the Newtonian approximation for the low mass range ($\leq 15M_{\odot}$) is acceptable at least for several ten ms after core bounce. In this study, our progenitor is a $15M_{\odot}$ star which is small among the mass range of CCSNe progenitors and thus, if we adopt much larger mass such as $\sim 40 - 100M_{\odot}$, the general relativistic effects become stronger and the qualitative differences may be appeared even in a similar time scale as those used in this report. Such high mass range calculations are now in progress and will be reported in near future.

To confirm the validation of numerical results, we have to connect them to the observations. One important observed object is the gravitational wave. Since we cannot observe directly in the vicinity of the center of CCSNe by the electro-magnetic wave, the gravitational wave is one of the limited ways with which we can observe directly. In this report, though we do not evaluate the gravitational wave forms, the non-axisymmetric motion and the bipolar configuration appear. These motions alter the gravitational wave forms as reported by Scheidegger et al. (2009) and we will examine the effects of, e.g., the progenitor mass or the non-axisymmetric motions or the magnetic field in the context of full general relativity. This will be our future work. Another object to confirm is the ejected elements accompanied with the explosions. CCSNe eject abundant heavy elements which are synthesized during the progenitor's main sequence age to their final fate and also during the explosion via, such as, r -process nucleosynthesis (Wanajo et al. 2002; Fujimoto et al.

2007; Kuroda et al. 2008). However, the ejected chemical compositions and abundances depend on the detailed properties of the explosion dynamics and we can still not explain the observed chemical abundances, one reason is due to the lack of comprehension about the explosion dynamics. By comparing our numerical results with the observations, we can feed back the observational studies to our numerical models and input physics.

Numerical computations were carried out on Cray XT4 at Center for Computational Astrophysics, CfCA, of National Astronomical Observatory of Japan. This work was partly supported by Grants-in-Aid for JSPS Fellows and for the Scientific Research from the Ministry of Education, Science and Culture of Japan (20105004). We are grateful to an anonymous referee for his/her valuable and constructive comments.

REFERENCES

- Acheson, D. J., 1979, *Solar Physics*, 62, 23
- Akiyama, S., Wheeler, J. C., Meier, D. L., & Lichtenstadt, I., 2003, *ApJ*, 584, 954
- Alcubierre, M. & Brügmann, B., 2001, *Phys. Rev. D*, 63, 104006
- Antón, L., Zanotti, O., Miralles, J. A., Martí, J. M., Ibáñez, J. M., Font, J. A., & Pons, J. A., 2006, *ApJ*, 637, 296
- Arnold, R., Deser, S., & Misner, C. W., 1962, "Gravitation: an introduction to current research", Louis Witten ed. (Wiley 1962), chapter 7, pp 227–265
- Balbus, S. A., & Hawley, J. F., 1991, *ApJ*, 376, 214
- Balsara, D. S., & Spicer, D. S., 1999, *Journal of Computational Physics*, 149, 270
- Balsara, D., 2001, *Journal of Computational Physics*, 174, 614
- Baumgarte, T. W., & Shapiro, S. L., 1999, *Phys. Rev. D*, 59, 024007
- Berger, M. J. & Colella, P., 1989, *Journal of Computational Physics*, 82, 64
- Blondin, J. M., Mezzacappa, A., & DeMario, C., 2003, *ApJ*, 584, 971
- Brio, M., & Wu, C. C., 1988, *J. Comput. Phys.*, 75, 400
- Burrows, A., Dessart, L., Livne, E., Ott, C. D. & Murphy, J., 2007, *ApJ*, 664, 416
- Cerdá-Durán, P., Font, J. A., Dimmelmeier, H., 2007, *A&A*, 474, 169
- Cerdá-Durán, P., Font, J. A., Antón, L., & Müller, E., 2008, *A&A*, 492, 937

- De Villiers, J. & Hawley, J. F., 2003, *ApJ*, 589, 458
- Duez, M. D., Marronetti, P., & Shapiro, S. L., 2003, *Phys. Rev. D*, 67, 024004
- Duncan, R. C., & Thompson, C., 1992, *ApJ*, 392, L9
- Etienne, Z. B., Faber, J. A., Liu, Y. T., Shapiro, S. L., Taniguchi, K. & Baumgarte, T. W., 2008, *Phys. Rev. D*, 77, 084002
- Fujimoto, S., Hashimoto, M., Kotake, K., & Yamada, S., 2007, *ApJ*, 656, 382
- Giacomazzo, B., & Rezzolla, L., 2006, *J. Fluid Mech.* 562, 223
- Hanawa, T., Mikami, H., & Matsumoto, T., 2008, *Journal of Computational Physics*, 227, 7952
- Harten, A., Lax, P. & van Leer, B., 1983, On upstream differencing and Godunov type methods for hyperbolic conservation laws. *SIAM review.* 25(1), pp 35-61
- Hawley, J. F., Smarr, L. L. & Wilson, J. R., 1984, *ApJ*, 277, 296
- Heger, A., Woosley, S. E. & Spruit, H. C., 2005, *ApJ*, 626, 350
- Hilbert, D., 1891, *Mathematische Annalen*, 38, 459
- Hirschi, R., Meyner, G. & Maeder, A., 2004, *A&A*, 425, 649
- Imamura, J. N., Pickett, B. K., & Durisen, R. H., 2003, *ApJ*, 587, 341
- Keil, W., Janka, H.-T., & Müller, E., 1996, *ApJ*, 473, L111
- Kiuchi, K., Shibata, M., & Yoshida, S., 2008, *Phys. Rev. D*, 78, 024029
- Kotake, K., Sawai, H., Yamada, S., & Sato, K., 2004, *ApJ*, 608, 391
- Komissarov, S. S., 1999, *MNRAS*, 303, 343
- Kuroda, T., Wanajo, S., & Nomoto, K., 2008, *ApJ*, 672, 1068
- Maeda, K., et al. 2008, *Science*, 319, 1220
- Matsumoto, T., 2007, *Publ. Astron. Soc. Japan.*, 59, 905
- Mikami, H., Sato, Y., Matsumoto, T., & Hanawa, T., 2008, *ApJ*, 683, 357
- Nakamura, T., Oohara, K. & Kojima, Y., 1987, *Progress of Theoretical Physics Supplement*, 90, 1
- Obergaulinger, M., Aloy, M.A., Dimmelmeier, H. & Müller, E., 2006, *A&A*, 457, 209
- Obergaulinger, M., Cerdà-Durà, P., Müller, E., & Aloy, M.A., 2009, *A&A*, 498, 241

- Ott, C. D., Ou, S., Tohline, J. E., & Burrows, A., 2005, *ApJ*, 625, L119
- Ott, C. D., Dimmelmeier, H., Marek, A., Janka, H.-T., Hawke, I., Zink, B. & Schnetter, E., 2007, *Phys. Rev. Lett.*, 98, 261101
- Ott, C. D., 2009, *Classical and Quantum Gravity*, 26, 204015
- Powell, K. G., Roe, P. L., Linde, T. J., Gombosi, T. I., & De Zeeuw, D. L., 1999, *Journal of Computational Physics*, 154, 284
- Press, W.H., Flannery, B. P., Teukolsky, S. A. & Vetterling, W. T., 1992, *Numerical Recipes in FORTRAN: The Art of Scientific Computing*, 2nd ed. Cambridge, England: Cambridge University Press, pp740-744
- Rampp, M., Müller, E., & Ruffert, M., 1998, *A&A*, 332, 969
- Ryu, D., Jones, T. W., & Frank, A., 1995, *ApJ*, 452, 785
- Sawai, H., Kotake, K., & Yamada, S., 2005, *ApJ*, 631, 446
- Scheidegger, S., Fischer, T., Whitehouse, S. C., & Liebendörfer, M., 2008, *A&A*, 490, 231
- Scheidegger, S., Käppeli, R., Whitehouse, S. C., Fischer, T., & Liebendörfer, M., 2009, *A&A*, 514, A51
- Schnetter, E., Hawley, S. H. & Hawke, I., 2004, *Classical and Quantum Gravity*, 21, 1465
- Shibata, M., & Nakamura, T., 1995, *Phys. Rev. D*, 52, 5428
- Shibata, M., 1997, *Phys. Rev. D*, 55, 2002
- Shibata, M., 1999, *Progress of Theoretical Physics*, 101, 1199
- Shibata, M., & Uryū, K., 2002, *Progress of Theoretical Physics*, 107, 265
- Shibata, M., Karino, S., & Eriguchi, Y., 2003, *MNRAS*, 343, 619
- Shibata, M., 2003, *ApJ*, 595, 992
- Shibata, M., & Sekiguchi, Y., 2005, *Phys. Rev. D*, 72, 044014
- Shibata, M., Liu, Y. T., Shapiro, S. L., & Stephens, B. C., 2006, *Phys. Rev. D*, 74, 104026
- Stone, J.M., & Norman, M.L., 1992, *ApJS*, 80, 753
- Takahara, M., & Sato, K., 1998, *ApJ*, 335, 301
- Takiwaki, T., Kotake, K., & Sato, K., 2009, *ApJ*, 691, 1360
- Tanaka, M., et al., 2009, *ApJ*, 692, 1131

- Tanaka, M., Kawabata, K. S., Maeda, K., Iye, M., Hattori, T., Pian, E., Nomoto, K., Mazzali, P. A., & Tominaga, N., 2009, *ApJ*, 699, 1119
- Teukolsky, S. A., 1982, *Phys. Rev. D*, 26, 745
- Thompson, C., & Duncan, R. C., 1993, *ApJ*, 408, 194
- Thompson, T. A., Quataert, E. & Burrows, A., 2005, *ApJ*, 620, 861
- Toro, E.F. 1999, *NUMERICA*, A Library of Source Codes for Teaching, Research and Applications. Numeritek Ltd., www.numeritek.com
- Truelove, J. K., Klein, R. I., McKee, C. F., Holliman II, J. H., Howell, L. H., Greenough, J. A. & Woods, D. T., 1998, *ApJ*, 495, 821
- Umeda, H., & Nomoto, K., 2008, *ApJ*, 673, 1014
- van der Vorst, H., 1992, *SIAM Journal on Scientific Computing*, 13, 631
- Van Leer, B., 1977, *Journal of Computational Physics*, 23, 263
- Wanajo, S., Itoh, N., Ishimaru, Y., Nozawa, S., & Beers, T. C., 2002, *ApJ*, 577, 853
- Watts, A. L., Andersson, N., & Jones, D. I., 2005, *ApJ*, 618, L37
- Wheeler, J. C., Meier, D. L., & Wilson, J. R., 2002, *ApJ*, 568, 807
- Yo, H.-J., Baumgarte, T. W., & Shapiro, S. L., 2002, *Phys. Rev. D*, 66, 084026
- Yoon, S.-C., & Langer, N., 2005, *A&A*, 443, 643
- Zlochower, Y., Baker, J. G., Campanelli, M. & Lousto, C. O., 2005, *Phys. Rev. D*, 72, 024021